Multifrequency Sp Stacking Reveals a Strong Asthenospheric Discontinuity beneath the Anatolian Region

JUNLIN HUA[1,1], Karen M Fischer[1,1], Mengxi Wu[1,1], and Nienke Blom[2,2]

[1]Brown University
[2]University of Cambridge

November 30, 2022

Abstract

This study presents an improved approach to common-conversion point stacking of converted body waves that incorporates scattering kernels, accurate and efficient measurement of stack uncertainties, and an alternative method for estimating free surface seismic velocities. To better separate waveforms into the P and SV components to calculate receiver functions, we developed an alternative method to measure near surface compressional and shear wave velocities from particle motions. To more accurately reflect converted phase scattering kernels in the common-conversion point stack, we defined new weighting functions to project receiver function amplitudes only to locations where sensitivities to horizontal discontinuities are high. To better quantify stack uncertainties, we derived an expression for the standard deviation of the stack amplitude that is more efficient than bootstrapping and can be used for any problem requiring the standard deviation of a weighted average. We tested these improved methods on Sp phase data from the Anatolian region, using multiple bandpass filters to image velocity gradients of varying depth extents. Common conversion point stacks of 23,787 Sp receiver functions demonstrate that the new weighting functions produce clearer and more continuous mantle phases, compared to previous approaches. The stacks reveal a positive velocity gradient at 80-150 km depth that is consistent with the base of an asthenospheric low velocity layer. This feature is particularly strong in stacks of longer period data, indicating it represents a gradual velocity gradient. At shorter periods, a lithosphere-asthenosphere boundary phase is observed at 60-90 km depth, marking the top of the low velocity layer.

New Approaches to Multifrequency Sp Stacking Tested in the Anatolian Region

J. Hua[1], K. M. Fischer[1], M. Wu[1] and N. A. Blom[2]

[1] Department of Earth, Environmental and Planetary Sciences, Brown University, Providence, RI 02906, USA.

[2] Bullard Laboratories, Department of Earth Sciences, University of Cambridge, Madingley Rise, Cambridge CB3 0EZ, UK.

Corresponding author: Junlin Hua (junlin_hua@brown.edu)

Key Points:

- A new approach to common conversion point stacking based on scattering kernels
- Fast and accurate quantification of the standard deviation of the weighted stack average
- Anomalously low velocity asthenosphere beneath Anatolia indicated by velocity discontinuities imaged with multifrequency data

Abstract

This study presents an improved approach to common-conversion point stacking of converted body waves that incorporates scattering kernels, accurate and efficient measurement of stack uncertainties, and an alternative method for estimating free surface seismic velocities. To better separate waveforms into the P and SV components to calculate receiver functions, we developed an alternative method to measure near surface compressional and shear wave velocities from particle motions. To more accurately reflect converted phase scattering kernels in the common-conversion point stack, we defined new weighting functions to project receiver function amplitudes only to locations where sensitivities to horizontal discontinuities are high. To better quantify stack uncertainties, we derived an expression for the standard deviation of the stack amplitude that is more efficient than bootstrapping and can be used for any problem requiring the standard deviation of a weighted average. We tested these improved methods on Sp phase data from the Anatolian region, using multiple bandpass filters to image velocity gradients of varying depth extents. Common conversion point stacks of 23,787 Sp receiver functions demonstrate that the new weighting functions produce clearer and more continuous mantle phases, compared to previous approaches. The stacks reveal a positive velocity gradient at 80-150 km depth that is consistent with the base of an asthenospheric low velocity layer. This feature is particularly strong in stacks of longer period data, indicating it represents a gradual velocity gradient. At shorter periods, a lithosphere-asthenosphere boundary phase is observed at 60-90 km depth, marking the top of the low velocity layer.

Plain Language Summary

This paper presents a new method that more accurately incorporates the physics of seismic scattering into how the wave records are combined to form images of gradients in seismic velocity structure. This method was tested on data from the Anatolian region, where the asthenosphere is known to have low seismic wave velocities, consistent with high mantle temperatures and possibly small fractions of partial melt, as suggested by the presence of

volcanic fields at the surface. However, the depth of the asthenospheric low velocity layer is not well known. In this study, we locate this low velocity mantle layer by applying the newly developed imaging method to seismic shear waves that convert to compressional waves at the velocity gradients that mark the layer boundaries. This study is the first to clearly resolve both the lower and upper margins of the asthenosphere for the whole region. The top of the layer corresponds to the lithosphere-asthenosphere boundary at 60-90 km depth, and this velocity gradient is localized in depth. However, the bottom boundary, which lies at depths of 80-150 km, occurs over a broader depth range.

1. Introduction

Teleseismic body waves that convert from S to P vibration (or vice versa) at velocity or density anomalies are potent tools for imaging velocity discontinuities in the crust and mantle. To isolate the effects of Earth structure, incident phases are often deconvolved from converted phases to remove source and instrument information, resulting in receiver functions (e.g. Farra & Vinnik, 2000) for Ps (incident P wave with converted S wave) and Sp (incident S wave with converted P wave) phases.

Common-conversion point (CCP) stacking of receiver functions (e.g. Dueker & Sheehan, 1997) is often used to image mantle discontinuities. During CCP stacking, converted waves are assumed to be generated around converted wave ray paths. Receiver function amplitudes recorded at surface stations are projected back along the paths, and the image is constructed by summing receiver function amplitudes as a function of position, assuming spatial functions that weight how a receiver function on a particular ray path contributes to the summed amplitude at a given location. In prior studies, these spatial functions are either represented by geographic bins of conversion points (e.g. Dueker & Sheehan, 1997; Kind et al., 2012; Rondenay, 2009), or by empirically defined weighting functions that represent Fresnel zones for vertically incident waves (e.g. Lekić & Fischer, 2017; Lekic et al., 2011; Wittlinger & Farra, 2007). However, to incorporate the physics of wave scattering into CCP stacking, these spatial functions should be consistent with the sensitivity kernels that describe how scattering from a point on a velocity discontinuity contributes to an observed converted phase, for example the scattering kernels for

Sp and Ps phases(e.g. Bostock & Rondenay, 1999; Bostock et al., 2001; Hansen & Schmandt, 2017; Hua et al., 2020; Mancinelli & Fischer, 2017). This condition is typically not met in prior CCP stacking approaches. Therefore, a new CCP stacking scheme is developed here based on the shape of scattering kernels while assuming that velocity structure is laterally invariant (Section 2.2).

High quality receiver functions are an essential ingredient of CCP stacking, and accurate incident and converted waveform components are necessary for robust receiver functions. While some studies deconvolve vertical from radial components to represent Ps receiver functions (e.g. Zor et al., 2003), others deconvolve P from SV. However, for Sp receiver functions, deconvolution of SV from P is necessary, due to the more horizontal incidence of Sp phases at the station (e.g. Kind et al., 2012). P and SV components are sometimes approximated using rotation of radial and vertical components into a ray-parallel and ray-normal reference frame (Kind et al., 2012), but, because the recorded seismogram is a combination of incident and reflected waves, other studies calculate P and SV components using the free-surface transform of Kennett (1991) (e.g. Abt et al., 2010; Bostock & Rondenay, 1999). This latter approach is more accurate in isolating incident and converted waveform components, but it requires values for near surface P and S velocities. Building on prior approaches (Abt et al., 2010; Park and Ishii, 2018) this study introduces a new method to accurately measure near surface P and S velocities from P and S particle motions in Section 2.1.

Accurate quantification of uncertainties in CCP stack amplitudes are critical to evaluating which features are robust and avoiding over-interpretation. The uncertainty is often quantified by the standard deviation of the stacked receiver function amplitude, for example as measured by bootstrapping (Hopper et al., 2014). During bootstrapping, individual receiver functions are randomly resampled and CCP stacked over multiple iterations, and the standard deviation of amplitude at each point among the multiple CCP stacks is calculated. However, this process is computationally expensive. In this study we derived a theoretical expression for accurately measuring the standard deviation of any weighted average and applied this to CCP stacking (Section 2.3), thus avoiding the need for bootstrapping.

These methodological improvements were tested by applying Sp receiver function CCP stacking to the upper mantle beneath the Anatolian region (Figure 1). Sp receiver functions were employed because they are not contaminated by crustal reverberations which affect Ps receiver functions in the time window where scattered waves from the shallow upper mantle arrive (Kind et al., 2012; Yuan et al., 2006). In addition, as will be shown in Section 2.2, the sensitivity kernels for Sp receiver functions are more effective at imaging quasi-horizontal upper mantle discontinuities with CCP stacking, particularly for the station spacing available in Anatolia (Figure 1).

The Anatolian region lies within the Alpine-Himalayan orogenic belt. In eastern Anatolia, collision between the Arabian and Eurasian plates began in the Oligocene, while central and western Anatolia have been escaping westwards, with their ongoing motion accommodated by the North Anatolian fault zone and the East Anatolian fault zone (e.g. Jolivet et al., 2013; Reilinger et al., 2006; Schildgen et al., 2014; A. M. C. Şengör et al., 2008). Numerous seismic models based on tomography with varied seismic phases have found thin lithosphere and low velocity asthenosphere beneath Anatolia, with particularly low velocities beneath eastern Anatolia; many models also contain dipping high velocity anomalies that have been interpreted as fragments of subducted lithosphere, with zones of lower velocity asthenosphere flowing between them (Bakırcı et al., 2012; Berk Biryol et al., 2011; Blom et al., 2020; Delph et al., 2015; Fichtner et al., 2013; Gans et al., 2009; Govers & Fichtner, 2016; Portner et al., 2018; Salaün et al., 2012; Wei et al., 2019; H. Zhu, 2018). Seismic models are typically consistent with the view that slab detachment occurred earlier beneath eastern Anatolia, creating a broad window filled with hot asthenosphere and surface uplift (Faccenna et al., 2006; Govers & Fichtner, 2016; Keskin, 2003; Schildgen et al., 2014; A. Şengör et al., 2003). Slab fragmentation and asthenospheric influx subsequently propagated west, contributing to uplift in central Anatolia (McNab et al., 2018; Schildgen et al., 2014). The particularly low velocity asthenosphere beneath eastern Anatolia is consistent with elevated mantle potential temperatures inferred from geochemical data (e.g. McNab et al., 2018; Nikogosian et al., 2018; Reid et al., 2017).

Constraints on seismic velocity interfaces from converted body waves have also illuminated the properties of the Anatolian crust and mantle. Numerous studies have focused on crustal properties (e.g. Abgarmi et al., 2017; Frederiksen et al., 2015; Karabulut et al., 2019; Licciardi et al., 2018; Ozacar et al., 2008; Vanacore et al., 2013; L. Zhu et al., 2006; Zor et al., 2003). However, two prior studies used Sp phases to image mantle discontinuities. Angus et al. (2006) found Sp phases consistent with a decrease in velocity over the lithosphere-asthenosphere boundary (LAB) at depths of 60-80 km in eastern Anatolia, whereas Kind et al. (2015) inferred LAB velocity gradients at 80-100 km across Anatolia. In this study, we re-visit Sp CCP stacking in the Anatolian mantle, enhanced by the methodological improvements described above and additional data, to refine constraints on lithospheric thickness and to search for mantle discontinuities associated with the base of the asthenosphere.

We first introduce the new method improvements (Section 2) and then describe the full process of data acquisition, processing and calculation of the CCP stack (Section 3). Key operations within each step of this process are briefly summarized in Figure 2. Results from the application of these methods to the Anatolian region, including the observation of an unusually strong positive velocity gradient at depths of 80-150 km, are discussed in Section 4.

2. Method Improvements

2.1. Free-surface Velocities and P-SV Phase Separation

The Sp receiver functions used in this study rely on accurate calculation of P and SV components from radial and vertical components based on a free-surface transform (Kennett, 1991) that removes the effect of free-surface reflection. The transform is expressed as

$$\begin{pmatrix} P \\ SV \end{pmatrix} = \mathbf{T}(\alpha^{FS}, \beta^{FS}, p) \begin{pmatrix} R \\ Z \end{pmatrix}, \quad \mathbf{T} = \begin{pmatrix} \dfrac{p(\beta^{FS})^2}{\alpha^{FS}} & \dfrac{(\beta^{FS})^2 p^2 - 0.5}{\alpha^{FS} q_\alpha} \\ \dfrac{0.5 - (\beta^{FS})^2 p^2}{\beta^{FS} q_\beta} & p\beta^{FS} \end{pmatrix}, \tag{1}$$

where R and Z are the recorded vertical and the radial components, P and SV are P and SV components before encountering the free-surface, $\mathbf{T}$ is the free-surface transform matrix, α^{FS} and β^{FS} are the assumed near-surface compressional velocity (V_p) and shear velocity (V_s), p is the ray parameter at the station in s/km, and $q_\alpha = [(\alpha^{FS})^{-2} - p^2)]^{0.5}$, $q_\beta = [(\beta^{FS})^{-2} - p^2)]^{0.5}$. Therefore, accurate estimation of α^{FS} and β^{FS} is required to perform the transform correctly.

Previously, Abt et al. (2010) also used equation (1) to obtain P and SV components for receiver function calculations, and they determined the free-surface velocities by performing a grid search over α^{FS} and β^{FS} using equation (1) to minimize SV in the P arrival window and P in the S arrival window. However, this method does not use the information in P for the P arrival, and information in SV for the S arrival. Other studies have investigated the free surface behavior of the polarization of the recorded phase (Wiechert & Zoeppritz, 1907) to better constrain α^{FS} and β^{FS} (Park & Ishii, 2018), and have used the frequency-dependence of the polarization to constrain local velocity stratification (Hannemann et al., 2016; Park et al., 2019; Svenningsen & Jacobsen, 2007). In this study, a new method is developed for estimating free-surface velocities. This method incorporates the behavior of P and SV at the free surface, including free surface reflections, but is not based on direct measurement of polarizations.

If the true P and SV components are expressed as P_0 and SV_0, and the true V_p and V_s are α_0^{FS} and β_0^{FS}, the recorded R and Z can be expressed as

$$\begin{pmatrix} R \\ Z \end{pmatrix} = \mathbf{R}(\alpha^{FS} = \alpha_0^{FS}, \beta^{FS} = \beta_0^{FS}, p) \begin{pmatrix} P_0 \\ SV_0 \end{pmatrix}, \quad \mathbf{R} = \frac{1}{q_\gamma^4 + 4p^2 q_\alpha q_\beta} \begin{pmatrix} \dfrac{4p\alpha^{FS} q_\alpha q_\beta}{(\beta^{FS})^2} & \dfrac{2q_\gamma^2 q_\beta}{\beta} \\ -\dfrac{2\alpha^{FS} q_\gamma^2 q_\alpha}{(\beta^{FS})^2} & \dfrac{4p q_\alpha q_\beta}{\beta} \end{pmatrix}, \quad (2)$$

where $q_\gamma = [(\beta^{FS})^{-2} - 2p^2)]^{0.5}$, and $\mathbf{R}$ is the reflection matrix containing reflection coefficients at the free surface (e.g. Aki & Richards, 2002), which is also the inverse matrix of $\mathbf{T}$. By substituting equation (2) into (1), the transformed P and SV components can be expressed as

$$\begin{pmatrix} P \\ SV \end{pmatrix} = \mathbf{T}(\alpha^{FS}, \beta^{FS}, p)\mathbf{R}(\alpha_0^{FS}, \beta_0^{FS}, p) \begin{pmatrix} P_0 \\ SV_0 \end{pmatrix}. \quad (3)$$

With equation (3), to solve for α_0^{FS} and β_0^{FS}, three particle motion patterns

$$\mathbf{C}_1(\alpha^{FS},\beta^{FS})=\frac{P\cdot SV}{R\cdot Z},\quad \mathbf{C}_2(\alpha^{FS},\beta^{FS})=\frac{P\cdot P}{R\cdot Z}\quad \text{and}\quad \mathbf{C}_3(\alpha^{FS},\beta^{FS})=\frac{SV\cdot SV}{R\cdot Z} \tag{4}$$

are first measured for both P and S arrivals (e.g. Figure 3). Specifically, P and SV are calculated from equation (1) for different α^{FS} (2.7-8.1 km/s with a 0.03 km/s increment) and β^{FS} (1.5-4.5 km/s with a 0.0167 km/s increment), and the patterns are then calculated using equation (4), making the observed patterns functions of α^{FS} and β^{FS}. The patterns include scaling by $R\cdot Z$ to normalize the amplitude of the patterns, so that the amplitude of the waveform does not affect the results. For the case of a half space with V_p=4.92 km/s and V_s=2.82 km/s and a P wave with a ray parameter of 0.0482 s/km, the three patterns based on propagator matrix synthetic seismograms (Keith & Crampin, 1977) are shown in Figures 3a to 3c, and the patterns for an SV wave with a ray parameter 0.1098 s/km are shown in Figures 3e to 3g.

After obtaining patterns from the observed waveforms, P and SV are then predicted for different α_0^{FS} and β_0^{FS} with equation (3) by setting $SV_0=0$ for the P arrival and $P_0=0$ for the S arrival, assuming the ray parameter of the real waveform. With the predicted P and SV, the three predicted patterns are calculated according to equation (4) and are labelled as $\mathbf{C}_1^p$, $\mathbf{C}_2^p$ and $\mathbf{C}_3^p$. The predicted patterns are not only functions of α^{FS} and β^{FS} but also α_0^{FS} and β_0^{FS}. Optimal α_0^{FS} and β_0^{FS} values are then obtained by matching $\mathbf{C}_1^p$, $\mathbf{C}_2^p$ and $\mathbf{C}_3^p$ for different α_0^{FS} and β_0^{FS} to $\mathbf{C}_1$, $\mathbf{C}_2$ and $\mathbf{C}_3$.

In practice, instead of using P and S arrivals together to constrain α_0^{FS} and β_0^{FS}, α_0^{FS} is obtained from S arrival pattern matching, and β_0^{FS} from P arrival pattern matching (Figures 3d & 3h). This choice is motivated by the fact that the P arrival polarization does not depend on α_0^{FS}, a result also shown in Park and Ishii (2018), and therefore the P arrival $\mathbf{C}_1$, $\mathbf{C}_2$ and $\mathbf{C}_3$ patterns also do not depend on α_0^{FS}. While the value of $\mathbf{C}_2$ does vary with α^{FS} in the P arrival $\mathbf{C}_2$ pattern (Figure 3b), the $\mathbf{C}_2$ pattern itself does not vary with values of α_0^{FS}. The independence of the P arrival $\mathbf{C}_1$, $\mathbf{C}_2$ and $\mathbf{C}_3$ patterns can be demonstrated as follows. From equations (1) and

(4), it can be shown that the $\mathbf{C}_1$, $\mathbf{C}_2$ and $\mathbf{C}_3$ patterns depend only on the polarization R/Z, and from equation (2), the polarization is expressed as

$$\frac{R}{Z}=\frac{\mathbf{R}_{11}P_0+\mathbf{R}_{12}SV_0}{\mathbf{R}_{21}P_0+\mathbf{R}_{22}SV_0}, \qquad (5)$$

where the subscripts refer to the row and column of an element in the $\mathbf{R}$ matrix. For the P arrival, $SV_0=0$, and the polarization $R/Z=-2pq_\beta/q_\gamma^2$ (equations 2 & 5). Therefore, the polarization is independent of α_0^{FS}. For the S arrival, $P_0=0$, and the polarization is equal to $q_\gamma^2/2pq_\alpha$ (equations 2 & 5), which depends on both α_0^{FS} and β_0^{FS}.

In practice, using P arrival patterns, a uniform grid search is performed over β_0^{FS}, with 181 values that range from 1.5 km/s to 4.5 km/s, to find the value that minimizes a misfit function defined as

$$\text{misfit}=\sqrt{\left\|\mathbf{C}_1-\mathbf{C}_1^p\right\|_2^2+\left\|\mathbf{C}_2-\mathbf{C}_2^p\right\|_2^2+\left\|\mathbf{C}_3-\mathbf{C}_3^p\right\|_2^2}, \qquad (6)$$

where the L_2-norm refers to the norm of a vector (i.e. treating $\mathbf{C}_1$ as a vector with 181×181 elements). We then use the β_0^{FS} value from this step together with the S arrival patterns to obtain α_0^{FS} by minimizing the same misfit function in equation (6), but through a grid search over α_0^{FS} with a minimum value of 2.7 km/s and a maximum value of 8.1 km/s.

This approach differs from that of Park and Ishii (2018) in two significant ways. First, Park and Ishii (2018) solve for free-surface velocities based on minimizing misfits between observed and predicted P incidence angles and S polarizations. In contrast, we minimize misfits between observed and predicted $\mathbf{C}$ patterns (equation 6), which are the normalized dot products of P and SV particle motions (equation 4). Second, Park and Ishii (2018) solve for free-surface P and S velocities simultaneously, while we first use equation (4) with P arrival data to solve for β_0^{FS} and then, with fixed β_0^{FS}, use equation (4) with S arrival data to solve for α_0^{FS}. Advantages of using only the P arrival patterns to solve for β_0^{FS} are that P phases typically have much higher signal-to-noise ratios than S phases, and trade-offs between α_0^{FS} and β_0^{FS} are to some extent reduced since P arrival patterns do not depend on α_0^{FS}.

The synthetic example in Figure 3 demonstrates the effectiveness of the pattern-matching method in finding α_0^{FS} and β_0^{FS}. For the grid search over β_0^{FS} using the P arrival, the estimated value of β_0^{FS} matches the free surface V_s from the model used to generate the synthetics (Figure 3d). In addition, while all the misfit components are minimized at the same value of β_0^{FS}, the $\mathbf{C}_2$ misfit dominates the total misfit relative to $\mathbf{C}_1$ and $\mathbf{C}_3$. This finding shows the advantage of the new method over the approach in Abt et al. (2010) which relied only on $\mathbf{C}_1$. For the S arrival, the grid search over α_0^{FS} yields a minimum misfit α_0^{FS} that matches V_p in the input model (Figure 3h). However, in this case $\mathbf{C}_1$, $\mathbf{C}_2$ and $\mathbf{C}_3$ all have substantial contributions to the total misfit, which again emphasizes the importance of using use all the patterns instead of relying only on $\mathbf{C}_1$ as in Abt et al. (2010).

To obtain free-surface velocities from multiple events at a single station, we first weight the velocity estimates by a value the describes the quality of the seismic phase, and then take the weighted mean of estimates for the station. One quality factor is a signal-to-noise ratio measured with moving signal and noise windows applied to the envelope function of Z for P arrivals, and to the envelope function of R for S arrivals. Signal-to-noise is defined as the average amplitude in the 5 s signal window divided by the average amplitude in the 20 s noise window, and the signal-to-noise of the phase (snr) is defined as the maximum signal-to-noise value within 25 s of the phase arrival time; phase arrival times were obtained using an array-based method (Lekić & Fischer, 2014). The second quality factor is the correlation coefficient ($corr$) of the R and Z components in a 3.5 s window around the phase arrival time. The weighting factor is equal to the product of these factors if snr is greater than 5 and $corr$ is greater than 0.95. Otherwise the weighting factor is set to zero and the phase is discarded. After obtaining individual β_0^{FS} values (equations 4 & 6) and their weights from P arrivals, the station free-surface shear velocity β_s^{FS} is defined as the weighted mean of the individual values. Assuming β_s^{FS}, individual α_0^{FS} measurements and their weights are obtained from S arrivals, and the station compressional velocity α_s^{FS} is calculated using a weighted average. If the number of non-zero weighted P arrivals is less than four, β_s^{FS} is set to 2.8 km/s, and if the number of non-zero weighted S arrivals is less than four, α_s^{FS} is set to $1.8\beta_s^{FS}$.

To show how the method works well with real data, the free surface velocity determination was applied to data from station ISP (GE network). The free-surface velocities α_s^{FS} and β_s^{FS} for this station are the same as the input velocity model used in the synthetic case in Figure 3. Figures S1a to S1c show the $\mathbf{C}_1$ - $\mathbf{C}_3$ patterns for a P arrival from an earthquake that occurred on 20 July 2014 at ~44.65°N, 148.78°E with a ray parameter equal to that of the P arrival in the synthetic case in Figure 3. The observed patterns are very similar to the synthetic patterns, except for $\mathbf{C}_3$ (Figure S1c) where the transformed SV component is not as successfully minimized as in the synthetic case. The misfit functions from the grid search result are also similar to those from the synthetic case (Figure 4a versus Figure 3d) with a β_0^{FS} of 2.82 km/s obtained at the minimum misfit. Values of β_0^{FS} were also obtained for P arrivals from other earthquakes, and their histogram is shown in Figure 5a. Although different arrivals resulted in different β_0^{FS} values, their distribution centers around the weighted mean for β_s^{FS} 2.82 km/s nearly symmetrically. The $\mathbf{C}_1$ - $\mathbf{C}_3$ patterns (Figure S1d to S1f) for an S arrival (from an earthquake that occurred on 18 May 2014 at ~4.25°N, 92.76°E with a ray parameter equal to that of the S arrival synthetic case in Figure 3) are similar to those from the synthetic case with minor differences. The grid search (Figure 4b) yields misfit functions that are similar to the synthetic case (Figure 3h), with an α_0^{FS} clearly defined at a value of 4.92 km/s. The distribution of α_0^{FS} values from different S arrivals shows greater variability than the β_s^{FS} distribution from the P arrivals (Figure 5b versus Figure 5a). This result is partly because the S polarization dependence on α_0^{FS} is weaker than on β_0^{FS} (Park & Ishii, 2018), and the number of P arrivals with non-zero weights is five times of the number of S arrivals with non-zero weights since P phases generally have a higher signal-to-noise ratio. Nonetheless, the α_0^{FS} distribution is still broadly centered around its weighted mean of 4.92 km/s.

After obtaining α_s^{FS} and β_s^{FS}, the P and SV components are calculated with equation (1) by setting $\alpha^{FS} = \alpha_s^{FS}$ and $\beta^{FS} = \beta_s^{FS}$. The P and SV components for the P and S arrivals employed in Figure 4 are plotted in Figures 4c and 4d. The SV component is minimal over the P arrival window, and the P component is minimal over the S arrival window, indicating the success of the transform with our new approach to finding free-surface velocities.

2.2. Kernel Based Common-Conversion Point Stacking

To better incorporate converted wave scattering into CCP stacking, we have developed spatial functions that describe how an individual Sp or Ps receiver function contributes to the stack, based on Sp and Ps sensitivity kernels (e.g. Hansen & Schmandt, 2017; Hua et al., 2020; Mancinelli & Fischer, 2017). During CCP stacking of Sp or Ps receiver functions, phase ray paths are traced to a given depth and the travel-time of the converted phase from that point to the station identifies the relevant amplitude from the receiver function. To calculate the stack at a given horizontal location for that depth, receiver function amplitudes are combined, assuming amplitude relationships between the location in the stack and the position of ray paths. In prior studies, these relationships have typically been described as geographic bins (e.g. Dueker & Sheehan, 1997) or with weighting functions based on vertical path Fresnel zones (e.g. Lekić & Fischer, 2017; Lekic et al., 2011; Wittlinger & Farra, 2007). Here we develop weighting functions that more accurately reflect the interaction of Sp and Ps phases with velocity structure using their sensitivity kernels.

The time-dependence of scattering can be illustrated by incident and scattered wave ray paths (Figure 6). An incident wave travels upward in the radial-vertical plane (*r-z* plane). The incident wave encounters a scatterer, a scattered wave is generated and propagates upward to the station, and it may not travel in the *r-z* plane. The incident wave travel time from the earthquake location to the station is defined as τ_i^r, and the incident wave travel time from the earthquake to the scatterer is defined as τ_i^s. The travel time of the scattered wave from the scatterer to the station is given as τ_j. The phase delay time between the scattered phase and the incident phase (equivalent to time in the receiver function) is described as

$$T = \tau_i^s + \tau_j - \tau_i^r . \quad (7)$$

Scatterers sharing the same T form the phase delay isochron (e.g. Bostock & Rondenay, 1999; Bostock et al., 2001). Energy from scatterers on the same isochron contributes to receiver function amplitude at the same time, and the isochrons determine the shape of the scattering kernels for receiver function amplitudes (e.g. Bostock & Rondenay, 1999; Bostock et al., 2001; Hansen & Schmandt, 2017; Hua et al., 2020; Mancinelli & Fischer, 2017). This formulation is based on the Born approximation that scattered waves will not be scattered again, so the travel time difference can be expressed as equation (7).

The shapes of the phase delay isochrons for Sp and Ps phases fundamentally differ. An Sp isochron is illustrated in Figure 7a. This example corresponds to a uniform half space with V_p=7.8 km/s and V_s=4.3 km/s (typical upper mantle values), an incident S wave ray parameter of 0.1098 s/km (same as used in Figures 4 & 5), and a 200 km scattering depth (the depth where the converted wave ray path intersects the isochron). For this case, the Sp isochron correponds to a delay time of -27.76 s. The isochron is horizontal near its minimum depth at the conversion point (the intersection point with the converted wave ray path), dips more steeply elsewhere, and extends to infinite distance. A Ps isochron is shown in Figure 7b, for an incident P wave ray parameter of 0.0482 s/km (same as used in Figures 4 & 5) and a scattering depth of 200 km. Here the Ps isochron correponds to a delay time of 21.74 s. The isochron is also horizontal around the conversion point, but this is the maximum depth on the isochron. In addition, the flat portion of the Ps isochron is much smaller than for the Sp isochron, the Ps isochron does not extend to infinite distance, and its slope angle can be as large as 90°.

Based on our knowledge of the isochrons, we developed a spatial weighting function for CCP stacking. The weighting function is based on the slope of the isochron, the geometrical distance from the scatterer to the station, and the depth offset between the scattering depth and the isochron. Each of these factors is discussed below.

An assumption inherent in CCP stacking is that velocity discontinuities are horizontal over the length scales where amplitudes from different individual converted phases (or receiver functions) are combined. To be consistent with converted phase sensitivity kernels, the amplitude weighting functions that describe these length scales should correspond to the portion of the isochron that is sensitive to horizontal structure, and what controls the sensitivity to discontinuity dip is the slope angle of the isochron (Rondenay et al., 2005). When a discontinuity overlaps with an isochron in space, scatterers on the discontinuity generate scattered waves that are recorded by the station at the same time, and the positive interference of the scattered waves produces a clear phase in the receiver function. Therefore, for CCP stacking, receiver function amplitudes should be projected into the stack along a depth interface only where their isochron slope angle is approximately 0°. This approach differs from migration methods that are designed to image discontinuities with an arbitrary dip angle and in which receiver function amplitude are projected along the whole isochron (e.g. Hua et al., 2020; Zhang & Schmandt, 2019).

The isochron slope angle is equal to the angle between the phase delay time gradient (∇T) and the vertical axis, and can be derived in a similar manner to Hua et al. (2020). From the path geometry in Figure 6, it can be seen that

$$\begin{aligned} &\frac{\partial \tau_i^s}{\partial r} = \frac{\sin\theta_i}{v_i}, \quad \frac{\partial \tau_i^s}{\partial t} = 0, \quad \frac{\partial \tau_i^s}{\partial z} = -\frac{\cos\theta_i}{v_i}, \\ &\frac{\partial \tau_j}{\partial r} = -\frac{\sin\varphi}{v_j}, \quad \frac{\partial \tau_j}{\partial t} = \frac{\sin\phi}{v_j}, \quad \frac{\partial \tau_j}{\partial z} = \frac{\cos\theta_j}{v_j}, \end{aligned} \tag{8}$$

where v_i is the incident wave velocity, v_j is the scattered wave velocity, θ_i is the angle from vertical of the incident wave path, θ_j is the scattered wave take-off angle, φ and ϕ are two angles defined in Figure 6. φ is positive when the scattered wave is traveling in the positive r direction, and ϕ is positive when the scattered wave is traveling in the negative t direction.

Because τ_i^r does not depend on the scatterer location, from equations (7) and (8), the gradient of T is expressed as

$$\nabla T = \left(\frac{\sin\theta_i}{v_i} - \frac{\sin\varphi}{v_j}\right)\mathbf{e}_r + \frac{\sin\phi}{v_j}\mathbf{e}_t + \left(\frac{\cos\theta_j}{v_j} - \frac{\cos\theta_i}{v_i}\right)\mathbf{e}_z \tag{9}$$

where $\mathbf{e}_r$, $\mathbf{e}_t$ and $\mathbf{e}_z$ are unit vector in *r*, *t* and *z* directions. From equation (9), and with some algebra, the slope angle ϑ is expressed as

$$\vartheta = \arctan\left(\frac{\sqrt{v_i^2 \sin^2\phi + \left(v_j \sin\theta_i - v_i \sin\varphi\right)^2}}{v_j \cos\theta_i - v_i \cos\theta_j}\right). \tag{10}$$

To simplify, φ and ϕ are replaced by the dihedral angle between the vertical plane of scattered wave propagation and the *r-z* plane (γ) through the geometric relationship

$$\sin\phi = \sin\theta_j \sin\gamma, \quad \sin\varphi = \sin\theta_j \cos\gamma, \tag{11}$$

where γ is positive when the scattered wave is traveling the positive *r* direction. By substituting equation (11) into (10), the slope angle is expressed as

$$\vartheta = \arctan\left(\frac{\sqrt{v_i^2 \sin^2\theta_j + v_j^2 \sin^2\theta_i - 2v_i v_j \cos\gamma \sin\theta_i \sin\theta_j}}{v_j \cos\theta_i - v_i \cos\theta_j}\right). \tag{12}$$

To obtain ϑ, v_i and v_j are taken from an existing velocity model, and γ is calculated as the difference between the earthquake back-azimuth and the azimuth from the station to the scatterer. Because teleseismic events are used, p, the ray parameter, is assumed to be invariant with horizontal location. Based on Snell's law, the incident wave vertical incidence angle is expressed as

$$\theta_i = \arcsin\left(\frac{v_i R_E p}{R_E - z}\right) \tag{13}$$

where R_E represents the earth radius, and z is the depth of the scatterer. To obtain θ_j, at each station, the 1D velocity structure traversed by the scattered phase is extracted from an existing velocity model, and 1000 rays whose ray parameters range from 0 s/km to the maximum value (i.e. the ray parameter for a horizontal wave at the surface) with a uniform increment are shot from the station. All points along each of the 1000 paths are labeled with their corresponding ray parameter, and scattered wave ray parameters for all locations in space can then be retrieved by interpolating the ray parameter relationship. θ_j is obtained by substituting the scattered wave ray parameter and v_j into equation (13).

To help visualize isochron slope angles, slope angle values from equation (12) are color-coded on the isochrons in Figure 7. The near-horizontal region is much larger on the Sp isochron than on the Ps case, even though the isochrons are sampling a horizontal discontinuity at the same depth. In contrast, the Ps isochrons have larger regions with steeper dips including significant near-vertical portions, explaining the ability of Ps receiver functions to image vertical discontinuities (e.g. Hansen & Schmandt, 2017). The slope angle distribution of points at 200 km depth for the Sp case in Figure 7a is shown in Figure 8a. The slope angle is minimized around the conversion point in a zone that is elongated in the *r* direction and symmetric about the *r* axis.

While isochrons control the overall shape of the scattering kernel, their overall amplitude is scaled by geometric spreading of the scattered wave from the scatterer to the station, and geometric spreading is to the first order inversely proportional to the geometric distance from the station to the scatterer (Hansen & Schmandt, 2017). Geometric distance from points at 200 km depth for the case in Figure 7 is shown in Figure 8b, where the smallest values lie below the station. During CCP stacking of Sp phases, although some points far from the station may have a relatively flat isochron, the receiver function amplitude should not make a significant contribution there because of the small geometric spreading value.

A third consideration is that receiver function amplitudes for a given converted wave ray path should not be projected to locations in the CCP stack where the depth offset between the isochron and the conversion point (e.g. the offset between the isochron and 200 km depth in Figure 7) is large. To estimate the depth offset at different locations, the slope angles of the isochron along the *r* axis (ϑ_r) and *t* axis (ϑ_t) are calculated based on the direction of ∇T in equation (9), and are expressed as

$$\vartheta_r = \arctan\left(\frac{v_i \sin\theta_j \cos\gamma - v_j \sin\theta_i}{v_j \cos\theta_i - v_i \cos\theta_j}\right), \quad \vartheta_t = \arctan\left(-\frac{v_i \sin\theta_j \sin\gamma}{v_j \cos\theta_i - v_i \cos\theta_j}\right). \tag{14}$$

The depth offset (Δz) is then estimated to the first order as

$$\Delta z = \tan \vartheta_r \Delta r + \tan \vartheta_t \Delta t \tag{15}$$

where Δr and Δt are the horizontal offsets from the imaging location to the conversion point in the *r* and *t* directions. For the case in Figure 7a, the true depth offset that is directly measured by calculating the depth difference between the isochron and 200 km depth is shown in Figure 8c, and the Δz estimate based on equation (15) is shown in Figure 8d. The first order values from equation (15) reflect the true depth offset reasonably well closer to the conversion point, but at more distant locations, equation (15) tends to overestimate the depth offset. However, because receiver function amplitudes should be projected to locations where the depth offset is small, such overestimation helps to make our stacking method more conservative.

A weighting function, W_1, was designed to limit the projection of receiver function amplitudes to stack locations with relatively flat isochrons, smaller distances to the station and smaller depth offset to the isochron.

$$W_1 = \frac{z}{d} \exp\left(-\frac{\vartheta^2}{2\sigma_\vartheta^2}\right) \exp\left(-\frac{\Delta z^2}{2\sigma_z^2}\right), \tag{16}$$

where z is the depth of the imaging point in the stack, and d is the geometrical distance from the station to the imaging point. σ_ϑ is a slope angle threshold, and at points with ϑ larger than σ_ϑ amplitudes are down-weighted. σ_z depth offset threshold, with a similar function relative to Δz. In practice σ_ϑ is chosen to be 5°, and σ_z is calculated by

$$\sigma_z = T_{RF} \frac{dz}{dT_j}, \tag{17}$$

where T_{RF} is the half-width of the Gaussian that is convolved with the receiver function during time-domain deconvolution (Ligorria & Ammon, 1999) to smooth the receiver function. T_j is the phase delay time (defined in the same way as T) along the converted wave ray path, while

dz/dT_j is the inverse of its vertical derivative. Therefore, σ_z characterizes the vertical imaging uncertainty that is introduced during receiver function generation.

Weighting functions are distorted ellipses that have their maxima at the conversion point and are elongated in the *r* direction. The Sp weighting function for the case in Figure 7a is illustrated in Figure 8e, while the weighting function for the Ps example is shown in Figure 8f. For mantle discontinuities at the same depth, the Ps weighting function occupies a much smaller area, indicating that CCP stacking without artificial interpolation or smoothing requires denser station spacing for Ps phases than for Sp. Because of the broader lateral extent of their weighting functions, CCP stacking of Sp phases is better suited to imaging near-horizontal discontinuities with stations spaced at more than 20-30 km. In addition, CCP stacking of Sp phases avoids artifacts related to crustal reverberations that are often strong features in Ps CCP images.

To calculate the CCP stack in practice, W_1 is set to zero where its value is less than 0.02 or the horizontal angular distance to the station is more than 10°. To weight all receiver functions equally, a normalized weighting function, W_2, is calculated as:

$$W_2 = \frac{W_1}{\sum_{horizontal} W_1}. \tag{18}$$

W_2 is simply W_1 divided by the sum of all W_1 at the same depth, so it would add up to one at each depth, and thus different receiver functions are weighted identically. At each imaging point, the CCP stacked receiver function amplitude (RF_s) can be expressed as

$$RF_s = \frac{\sum_k (W_2)_k RF_k}{\sum_k (W_2)_k}, \tag{19}$$

which is the weighted average of individual receiver function amplitudes (RF_k) from different records, and the subscript k refers to the index of the individual record.

2.3. The Standard Deviation of a Weighted Average

In order to interpret a CCP stack, knowledge of the uncertainties in the stack amplitude are necessary to assess which structural features have amplitudes that exceed the uncertainty threshold. In some previous studies, the stack amplitude uncertainty was estimated by bootstrapping the CCP stacking process (e.g. Hua et al., 2018). The CCP stack was constructed multiple times based on random samples of the receiver functions, and these individual stacks were represented by their bootstrap mean at each point, with the bootstrap standard deviation at each point indicating the uncertainty. However, receiver functions often number in the tens of thousands, with thousands of receiver functions contributing to each image point. This volume of data requires a very large number of CCP stack iterations to get a reliable standard deviation from bootstrapping, resulting in a high computational cost. Therefore, we have developed a new approach to measuring the standard deviation of a weighted average. In particular, this approach is appropriate for cases where the sums of the weights are allowed to vary while the weights themselves could be dependent on the sample.

For a weighted average in the same form as equation (19), when the number of samples (n) is large enough, the central limit theorem indicates that the weighted average of a random sample can be expressed as

$$\frac{\sum wx}{\sum w} = \frac{\frac{1}{n}\sum wx}{\frac{1}{n}\sum w} \cong \frac{\mu_{wx} + \frac{1}{\sqrt{n}}\sigma_{wx}\varepsilon_1}{\mu_w + \frac{1}{\sqrt{n}}\sigma_w\varepsilon_2}, \tag{20}$$

where w is the weight and x is the sample value, μ_{wx} and μ_w stand for expected values of wx and w, σ_{wx} and σ_w are standard deviations for wx and w, and both ε_1 and ε_2 follow the normal distribution $N(0,1)$. For equation (20) to be valid, samples are required to be independent and with the same distribution, and the same is true for the weights. However, the weights do not necessarily need to be independent of the samples. When n is large enough, equation (20) can be approximated by a Taylor expansion as

$$\begin{aligned}\frac{\mu_{wx}+\frac{1}{\sqrt{n}}\sigma_{wx}\varepsilon_1}{\mu_w+\frac{1}{\sqrt{n}}\sigma_w\varepsilon_2} &= \frac{1}{\mu_w}\left(\mu_{wx}+\frac{1}{\sqrt{n}}\sigma_{wx}\varepsilon_1\right)\left[1-\frac{1}{\sqrt{n}\mu_w}\sigma_w\varepsilon_2+O\left(\frac{1}{n}\right)\right] \\ &= \frac{1}{\mu_w}\left[\mu_{wx}-\frac{\mu_{wx}}{\sqrt{n}\mu_w}\sigma_w\varepsilon_2+\frac{1}{\sqrt{n}}\sigma_{wx}\varepsilon_1+O\left(\frac{1}{n}\right)\right]\end{aligned}, \tag{21}$$

The first term in the bracket characterizes the expectation of the average, while the other two terms characterize the variability of the weighted average. Therefore, the expectation (E) and the variance (V) of the weighted average are expressed as

$$\begin{aligned}E\left(\frac{\sum wx}{\sum w}\right) &= \frac{\mu_{wx}}{\mu_w} \\ V\left(\frac{\sum wx}{\sum w}\right) &= \frac{1}{n\mu_w^2}V\left(\sigma_{wx}\varepsilon_1-\frac{\mu_{wx}}{\mu_w}\sigma_w\varepsilon_2\right) \\ &= \frac{1}{n\mu_w^2}\left[\sigma_{wx}^2+\frac{\mu_{wx}^2}{\mu_w^2}\sigma_w^2-\frac{2\mu_{wx}}{\mu_w}\sigma_{wx}\sigma_w Corr\left(\varepsilon_1,\varepsilon_2\right)\right]\end{aligned}, \tag{22}$$

and the correlation $Corr$ can be expressed as

$$Corr\left(\varepsilon_1,\varepsilon_2\right)=Corr\left(\sum wx,\sum w\right)=\frac{Cov\left(\sum wx,\sum w\right)}{\sqrt{V\left(\sum wx\right)V\left(\sum w\right)}} \tag{23}$$

based on the central limit theorem (equation 20), where Cov stands for covariance. The sample covariance $Cov\left(\sum wx,\sum w\right)$ is equal to n times the population covariance $Cov\left(wx,w\right)$, since Cov is a bilinear operator and samples are independent. The correlation in equation (23) can be further derived as

$$Corr\left(\varepsilon_1,\varepsilon_2\right)=\frac{nCov\left(wx,w\right)}{\sqrt{n^2V\left(wx\right)V\left(w\right)}}=\frac{Cov\left(wx,w\right)}{\sigma_{wx}\sigma_w}, \tag{24}$$

In practice, μ_{wx}, μ_w, σ_{wx}, σ_w and $Cov(wx,w)$ can be estimated from samples as

$$\mu_{wx} = \overline{wx}, \quad \mu_w = \overline{w}, \quad \sigma_{wx} = \sqrt{\overline{w^2x^2} - \left(\overline{wx}\right)^2}, \quad \sigma_w = \sqrt{\overline{w^2} - \left(\overline{w}\right)^2}, \quad Cov(wx, w) = \overline{w^2x} - \overline{wx}\,\overline{w}, \tag{25}$$

where the bar indicates the sample average. By substituting equations (24) and (25) into equation (22), and after some algebra, the standard deviation (Std) of the weighted average, which is the square root of the variance in equation (22), can be expressed as

$$Std\left(\frac{\sum wx}{\sum w}\right) = \frac{\sqrt{\left(\sum w^2x^2\right)\left(\sum w\right)^2 + \left(\sum w^2\right)\left(\sum wx\right)^2 - 2\left(\sum w\right)\left(\sum wx\right)\left(\sum w^2x\right)}}{\left(\sum w\right)^2}, \tag{26}$$

In the case of CCP stacking, where x is receiver function amplitude and w is W_2, equation (26) characterizes the uncertainty of stack amplitude at each point in the stack volume. However, this expression can also be applied to any weighted mean where samples are independent but drawn from the same distribution, and weights are independent but drawn from the same distribution.

To show the effectiveness of the standard deviation expression in equation (26), a numerical experiment was designed. We randomly generated 648 samples based on a normal distribution $N(0.02, 0.08^2)$, and the corresponding weights were randomly generated based on a normal distribution $N(0.7, 0.4^2)$. The histograms of the resulting samples and weights are shown in Figures 9a and 9b, and the standard deviation of the weighted mean of these data from equation (26) is shown by the black line in Figure 9c. For comparison, 50,000 iterations of bootstrapping were also performed on these data. In each iteration, 648 random values were drawn from the samples and weights, and their weighted average was calculated. After each iteration, the estimated standard deviation of the weighted averages based on the last and all previous iterations was calculated. For this case, the bootstrapped standard deviation starts to converge to a stable value after ~1,000 iterations, and the value it converges to is very close to the weighted standard deviation from equation (26) which is based on only one calculation. To show how these standard deviation estimates compare to the true standard deviation, a Monte Carlo simulation was designed. Instead of using one set of sample and weights (Figures 9a & 9b) as in the bootstrap case, at every iteration, a new set of sample and weights was generated based on the true distribution, and the weighted average was calculated. Then, the standard deviation calculated from the last on all previous sets of sample and weights was stored. The weighted standard deviation from the Monte Carlo simulation converges to a value which should approximate the true standard deviation (Figure 9c). This value is close to the equation (26) weighted standard deviation, but is offset by a small amount, because the single set of samples and weights used in equation (26) does not strictly follow the overall distributions. However, the good agreement between the estimate from equation (26) and both the true and bootstrap standard deviations demonstrates the accuracy of the much more efficient equation (26) approach.

We also compared the weighted standard deviation from equation (26) to the bootstrap standard deviation from the receiver function data in the real CCP stack (Figure 9d). In this example, for an imaging point located at 40.5°N, 38°E and 125 km depth, there are 648 individual receiver functions that have non-zero W_2 (equation 18). However, because in practice bootstrapping of the CCP stack would be performed over all 23,787 receiver functions, the sample size in this example is 23,787, although only 648 samples have non-zero weights. Again the weighted standard deviation from equation (26) equals the value to which the bootstrapping converges, although in this case reasonable convergence requires ~600 iterations.

Therefore, the approach summarized in equation (26) is an accurate and computationally fast means of calculating the standard deviation of a weighted average, and is applicable to CCP stacking, but also to a wider range of problems. This approach is especially suitable for problems where the sum of the weights is not fixed, since a much simpler expression can be used when the sum is fixed. For example, equation (26) can also be used to quantify the standard deviation of the measured free-surface velocity in Section 2.1. In addition, equation (26) is also powerful in the sense that it does not require the weight to be independent of the sample value, since the correlation between the weighted sum and the sum of the weights (equation 24) is considered in the derivation.

3. Data Processing and CCP Stacking

Data used in this study are Sp phases from broadband seismograms recorded from as early as 1990 to 2019 by 453 seismic stations around the Anatolian region (Figure 1) available from the International Federation of Digital Seismograph Networks (FDSN). Among all the stations, 153 of them are permanent stations from the network KO (Kandilli Observatory and Earthquake Research Institute Bosphorus Univ., 2001). Other contributing stations consist of 58 permanent stations from 10 networks (GE, HL, TU, CQ, HT, GO, HC, MN, IU, AB) and 242 temporary stations from 14 networks (YB, YL, YI, XW, XY, Z3, ZZ, XO, XH, YF, TK, SU, SD). Network references appear in the Acknowledgements.

Seismic records were retrieved for earthquakes with epicentral distances between 30° and 90° and a minimum moment magnitude of 5.8. To determine appropriate phase windows for P and S arrivals, the arrival time of the phases was picked using an array-based method (Lekić & Fischer, 2014) that results in more robust phase identification than from individual records. The seismograms were then filtered by a 4-100 s bandpass filter, and the free-surface velocities are calculated based on the method described in section 2.1. In addition, 2-20 s and 10-100 s bandpass filters were also used to help better detect different velocity structures, and will be discussed in section 4. After retrieving the free-surface velocities, the P and SV components of the seismic records were calculated from equation (1). The signal-to-noise ratios of the S phases were then measured from the SV component, using the ratio of the mean amplitude in a 5 s signal window to the mean amplitude in a 25 s noise window.

Sp receiver functions were then obtained by deconvolving the SV component of the direct S arrival from the P component which contains the Sp precursors. Deconvolution was performed using a time-domain deconvolution method (Ligorria & Ammon, 1999). The resulting impulse responses were convolved with a Gaussian whose half-width is 1 s and whose peak value is 1. However, while P and S phases from all distances were used for measuring the free-surface velocity, only earthquakes with epicentral distances between 55° and 85° were used to generate Sp receiver functions. We then eliminated receiver functions with a signal-to-noise ratios of less than two, or for which the difference between the arrival time determined from the array-based method and the prediction of the AK135 reference model (Kennett et al., 1995) is more than 10 s. With these criteria, 66,693 Sp receiver functions were generated.

To migrate the receiver functions to depth, we used 1D velocity models that reflect velocity along the converted P phase ray path from the recent full-waveform inversion model (Blom et al., 2020). Using a model derived from full-waveform inversion is advantageous because absolute velocities are inverted for directly, and because this method is especially well suited for areas with significant heterogeneity such as Anatolia. For stations outside the limits of the velocity model, the velocity at the closest location was used. Instead of directly using V_p from Blom et al. (2020), we calculated the average V_p / V_s at every depth in the study region (33°-45°N and 23°-48°E) and used the average V_p / V_s multiplied by V_s to obtain V_p. V_s is better-resolved than V_p in the model of Blom et al. (2020) for two reasons. First, because V_s is always lower than V_p, sensitivity kernels for this parameter are more spatially constrained than those for V_p and thus contain more detail. Second, full-waveform inversion models are dominated by surface waves, which naturally have stronger sensitivity to V_s. Our approach avoids zones with unrealistic V_p/V_s values due to this heterogeneous sensitivity. The V_s model used in this paper for migration is the shear velocity model corresponding to SV particle motion.

A range of criteria were applied to the migrated receiver functions to eliminate outliers. A prominent Moho is evident across the study region both in this study and in prior work (e.g. Abgarmi et al., 2017; Frederiksen et al., 2015; Karabulut et al., 2019; Licciardi et al., 2018; Ozacar et al., 2008; Vanacore et al., 2013; L. Zhu et al., 2006; Zor et al., 2003). Since the Moho predicts strong negative phases in Sp receiver functions, we discarded receiver functions without such signals at shallow depths. Receiver function negative amplitudes in the range from 15 km to 60 km depth were used to form a vector $\mathbf{rf}_{sn}$, and receiver functions with $\|\mathbf{rf}_{sn}\|_2^2$ smaller than 20% of the median $\|\mathbf{rf}_{sn}\|_2^2$ from all receiver functions were discarded. In addition, using positive amplitudes between 15 km and 60 km depth to form the vector $\mathbf{rf}_{sp}$, receiver functions with $\|\mathbf{rf}_{sp}\|_2^2$ greater than 3 times the median $\|\mathbf{rf}_{sp}\|_2^2$ from all receiver functions were discarded. With these two Moho related quality control criteria, receiver functions without obvious Moho phases are removed (second and third columns in Figure S2).

Other criteria remove receiver functions with large and physically non-plausible amplitude variations. Receiver function amplitudes predicted by the Blom et al. (2020) model provide a reasonable benchmark for plausible receiver function amplitudes. For the minimum, median and maximum S wave ray parameters of all seismic records, synthetic seismograms were calculated for Vs as a function of depth from Blom et al. (2020) at 1° horizontal increments, using the propagator matrix method (Keith & Crampin, 1977). Receiver functions were generated from the synthetic waveforms using the same approach that was applied to the data. From the synthetic receiver functions for the entire study region, the minimum ($\mathbf{rf}_{\min}$) and maximum ($\mathbf{rf}_{\max}$) amplitudes were found, together with their mean value ($\mathbf{rf}_{mean}$). The half-width of the amplitude range $\mathbf{rf}_{hw}$ was defined as $(\mathbf{rf}_{max} - \mathbf{rf}_{min})/2$. To eliminate observed receiver functions ($\mathbf{rf}$) with abnormally large amplitudes, receiver functions with $\|\mathbf{rf} - \mathbf{rf}_{mean}\|_2^2$ greater than five times the median $\|\mathbf{rf} - \mathbf{rf}_{mean}\|_2^2$ from all receiver functions were discarded. This criterion only discards receiver functions that have enormously large amplitudes, and the number of receiver function removed by this step is relatively small (fourth column in Figure S2). However, it is a useful tool to eliminate obviously unrealistic receiver functions, for example cases with a single huge peak near zero time that typically reflect bad data. In addition, to remove sustained large amplitudes in the mantle which are completely inconsistent with Blom et al. (2020) model, depth layers greater than 60 km where the receiver function amplitude $\mathbf{rf}$ is either smaller than $\mathbf{rf}_{mean} - 0.8\mathbf{rf}_{hw}$ or larger than $\mathbf{rf}_{mean} + 0.8\mathbf{rf}_{hw}$ were counted, with their number indicated as n_d. We then discarded all receiver functions with n_d larger than the median of n_d from all receiver functions. The n_d criterion is the strictest test we applied, as it removes half of the data, and it significantly reduces noise in the mantle depth range (fifth column in Figure S2).

With these four quality control criteria, unrealistic receiver functions are effectively removed (sixth column versus first column in Figure S2). However, the same primary phases appear in the stack in all cases, and the only significant change is that adding any one of the other criteria (columns two to four in Figure S2) to the initial signal-to-noise threshold (column one in Figure S2) increases the amplitude of the phase at depths of 100-150 km in this location.

CCP stacking was applied to the remaining 23,787 receiver functions (as described in Section 2.2), and the stack uncertainties were calculated (Section 2.3). The conversion points at 125 km depth (Figure 10) illustrate that much of the Anatolian region is sampled by the measurements. At each node in a grid with 0.1° spacing horizontally and 0.5 km spacing in depth, the migrated receiver functions were stacked based on equation (19), and the standard deviation of the stacked result was estimated by equation (26). To quantify the amount of receiver function information at each point in the stack, the weights for individual receiver functions at the same node were summed $\sum W_2$ (equation 18) to obtain a value called W_s. Only features with relatively large W_s were interpreted, partly to ensure sufficient data were used for the stacking at the place, and partly because the standard deviation formulation (equation 26) is only valid when the number of samples is large enough. However, because receiver functions were not projected to depths where the ray parameter is larger than the critical ray parameter of the P wave, the horizontal sum of W_s at greater depths is always smaller than the sum at smaller depths. Therefore, in order to eliminate bias due to this effect, W_s is normalized to a new depth-insensitive weighting W_3 as

$$W_3 = \frac{W_s}{\sum_{horizontal} W_s} \cdot \frac{\left(\sum_{vertical} \sum_{horizontal} W_s \right)}{n_{layer}}, \tag{27}$$

where n_{layer} is the number of depth layers (901 in this study). CCP stacking results were only interpreted at points with W_3 over 0.4. The W_3 distribution of the region at 125 km depth is shown in Figure 10, and for most of the continental Anatolian region W_3 exceeds the 0.4 threshold for interpretation. In addition, the CCP stack is interpreted only if the standard deviation is less than 0.01 or less than half of the weighted and stacked receiver function amplitude.

As an example, the CCP stack on profile A-A', which crosses the Anatolian region from east to west (Figure 11a), indicates a Moho that is partially imaged (red phase at 30-50 km depth), a 410-discontinuity that extends across most of the profile, and a negative velocity gradient at depths of 360-370 km that has been observed elsewhere and interpreted as the top of a low velocity layer just above the 410-discontinuity (e.g. Vinnik & Farra, 2002). We also observe a prominent mantle arrival at depths of 80-150 km, indicative of a velocity increase with depth, that will be discussed further below. A weak positive velocity gradient is also observed around 250 – 300 km depth in some locations. Figure 11b shows that the standard deviation of the profile is typically small and uniform below 100 km depth. However, the standard deviation above 50 km is much larger, even at points with large W_3 (Figure 11c), and cannot be interpreted except at points where the Moho Sp phase has a large enough amplitude to exceed twice of the large standard deviation. Unlike the standard deviation, the W_3 weight distribution is highest along groups of dense converted P ray paths and is larger overall above 300 km depth (Figure 11c). Because most of the events are from the northeast to east (Figure 10b), deep structures beneath the west end of the profile are not well imaged and are not shown due to small weight values (Figure 11a).

4. Results and Discussion

To show how the kernel based CCP stacking method introduced in section 2.2, the free-surface velocity determination method introduced in section 2.1, and the chosen velocity model influence the CCP stacking results, we calculated the CCP stack for three additional cases. In the first, we used the same collection of receiver functions, but with the stacking method in Hua et al. (2018), which employed an empirical weighting function defined by a vertical ray Fresnel zone similar to that in Lekić and Fischer (2017) assuming a dominant frequency of 13 s. The result for cross-section A-A' appears in Figure 12a, but because the weighting function here is defined differently from the weighting function in section 2.1, the image is shown where W_3 is more than 40 instead of 0.4. While the same major phases (Moho, 410 discontinuity, negative amplitudes at 80-150 km) appear in both cases, in the kernel based CCP stacking (Figure 11a) they are more continuous, and the rest of the image contains less small-scale variation in amplitude. This improvement is likely the result of the more physically correct weighting function in the kernel-based stack that individually determines the sensitivity to horizontal discontinuities for each individual receiver function and enables them to more correctly interfere at the appropriate location.

We also tested the improvement in the clarity of the CCP stack from the new approach to determining free-surface velocities. In this case (Figure 12b) we use the same set of receiver functions and the older stacking method used in Figure 12a, but with the free surface velocity determination method used in Hopper et al. (2014) which is essentially that of Abt et al. (2010). The differences between the two cases are subtle, but the more accurately determined free surface velocities use in Figure 12a result in slightly different amplitudes for the negative phase at 80-150 km depth. This comparison suggests that the new approach provides only an incremental improvement. Nonetheless, more accurately constrained free surface velocities contribute confidence to the CCP stack, and in addition they are a valuable tool for studying near surface structures (e.g. Park & Ishii, 2018; Park et al., 2019). In addition, this test also indicates that even if free-surface velocities are not estimated very precisely, their influence on mantle CCP stacking is likely not large as long as the values are reasonably accurate.

To verify that the velocity model we chose (Blom et al., 2020) to migrate the receiver functions and calculate the CCP stack does not overly influence the CCP stack results, we also employed the kernel based CCP stacking with the velocity model for Anatolia from Fichtner et al. (2013). However, in this case we directly used both V_p and V_s given by the model. The results of this case (Figure 12c) are similar to those obtained when using Blom et al. (2020) (Figure 11a). Noticeable differences are that the negative phase at 80 – 150 km depth is slightly stronger at ~36°E when using Fichtner et al. (2013), but more continuous at 38°E-39°E with Blom et al. (2020), and the 410 discontinuity is in general more continuous with Blom et al. (2020), while a shallower 410 discontinuity is evident at 33-39 °E when using Fichtner et al. (2013). However, these differences are relatively minor, and the overall agreement indicates that the CCP stack structures are not dramatically influenced by the assumed velocity model.

To further explore how data quality criteria influence the CCP stack, we performed the kernel based CCP stacking with the quality control criteria that remove receiver functions with absent Moho phases (Section 3), as well as the signal-to-noise threshold of 2. The Moho criteria relate only to receiver function amplitudes above 60 km depth, so mantle phases do not influence the quality measure. After applying these criteria, 45,872 receiver functions were retained for stacking. This stack contains nearly twice the number of receiver functions used in the final stack, and the individual receiver functions exhibit greater scatter (second and third columns versus the sixth column in Figure S2). Nonetheless, this stack (Figure S3) contains phases similar to those in the final stack (Figure 11a). One difference is that the negative phases at 80-150 km depth are more coherent with stricter quality criteria (Figure 11a) than in the case with only the Moho criteria (Figure S3). This difference is particular noticeable at 38°E-39°E, although it is reversed at 41°E-43°E. Because the receiver functions removed by the stricter criteria contain physically unrealistic energy, we focus our interpretation on the final stack.

The negative Sp phase at depths of 80 – 150 km persists widely beneath Anatolia, regardless of the stacking method and migration velocity model. Unlike the Moho and 410 discontinuity, which are expected globally, the negative upper mantle discontinuity is a more unusual feature. This negative Sp phase, which corresponds to a shear velocity increase with depth, is broadly consistent with V_s gradients in the model of Blom et al. (2020). The depth of the Sp phase (Figure 11a) lies near the base of a layer that is dominated by low velocities in the Blom et al. (2019) model (Figure 13a). The calculated vertical V_s gradients Blom et al. (2020) (Figure 13b) agree with the overall position of the negative Sp phase at longitudes of 31°E to 41°E, and from 41°E to 44°E, where the CCP stack only shows only weak negative Sp energy that is distributed over a broad range of depths (Figure 11a), vertically-localized positive velocity gradients are also not clearly observed in the velocity model (Figure 13b). However, some features disagree. For example, the positive velocity gradient at 200 km depth from 30°E to 32°E in the Blom et al. (2020) model is not matched clearly by a feature in the CCP stack. Comparison of the CCP stack with V_s and the vertical V_s gradient from Fichtner et al. (2013) (Figures S4a and S4b) show a similar level of agreement. All shear velocity profiles from full-waveform tomography models in this study (Figures 13, S4 & S5) correspond to SV velocity.

The widespread presence of the negative Sp phase at depths of 80 – 150 km is demonstrated by other cross-sections through the CCP stack. Cross-section B-B' (Figure 14a) which is south of A-A' also contains the negative Sp phase at 80 – 150 km depth from 29°E to 40°E, as well as from 42°E to 44°E beneath eastern Anatolia. The phase is also observed in north-south striking cross-sections (Figure 15), and it extends from 38°N to 40.5°N in the west (Figure 15a), from at least 37°N to 41°N in central-eastern Anatolia (Figure 15b), and from 37.5°N to 41.5°N in part of easternmost Anatolia (Figure 15c). However, the phase is not strong ubiquitously. Its amplitude and continuity are strongly diminished in much of the region north of 41°N-41.5°N, as shown in Figures 15a and 15b, and in the east-west cross-section C-C' (Figure 14c). This decrease in the amplitude of the negative Sp phase north of the plate boundary broadly correlates with a reduction of the intensity of the low velocity layer whose base it marks, as shown by a comparison of the Blom et al. (2019) shear velocity model on profiles B-B' (Figure S5a) and A-A' (Figure 13) versus C-C' (Figure S5b). A similar trend appears in the shear velocity models of Fichtner et al. (2013), and a third full-waveform inversion that spans Anatolia (H. Zhu, 2018). Lack of Sp data in the northeast corner of the study region limit our ability to assess the northward limit of negative phase amplitudes as far east as 44°E (Figure 15c). However, some waveform inversion models indicate that very low velocity asthenosphere extends further north at longitudes east of approximately 42°E-43°E, relative to the rest of the study region (Blom et al., 2020; H. Zhu, 2018).

The spatial distribution of the negative Sp phase, which appears to mark the base of the asthenospheric low velocity zone, differs from the results of prior Sp studies in the region. The Sp receiver function study by Kind et al. (2015) showed evidence for positive velocity gradients in shallow upper mantle, but the depths where this energy was observed do not always match our results. In Angus et al. (2006), positive velocity gradients were not observed from Sp phases in the 90-150 km depth range. However, much of the region sampled in Angus et al. (2006) lies in eastern Anatolia where the Sp CCP stack presented here shows only a weak positive Sp arrival (e.g. 40°E to 43°E in Figures 11a & 14a), indicating that this study and our results are not incompatible.

The anomalously low velocity asthenosphere beneath Anatolia, whose lower margin is indicated by the negative Sp phase, is observed by many seismic studies. In addition to the full-waveform inversion studies described above (Blom et al., 2020; Fichtner et al., 2013; H. Zhu, 2018), low velocity asthenosphere is also observed beneath the Anatolian region by surface wave tomography (Bakırcı et al., 2012; Salaün et al., 2012) and P wave tomography (Portner et al., 2018; Wei et al., 2019). Prior studies also found low Pn wave velocity (Gans et al., 2009; Mutlu & Karabulut, 2011) and high Sn wave attenuation (Gök et al., 2003) beneath a large portion of Anatolia. All of these studies are consistent with anomalously high mantle temperatures, which have also been indicated by multiple geochemical studies (McNab et al., 2018; Nikogosian et al., 2018; Reid et al., 2017). In addition, elevated mantle V_p/V_s ratios (H. Zhu, 2018) as well as the presence of young magmatism (<10 Ma) across the study region (McNab et al., 2018; Nikogosian et al., 2018; Reid et al., 2017) indicate that low velocities in the asthenospheric layer could be enhanced by the presence of partial melt, leading to unusually strong negative Sp energy from the base of this layer. Other regions with a negative Sp arrival in the shallow upper mantle are also often zones of active or recent magmatic activity where the phase could mark the base of a melt-rich mantle layer (e.g. Ford et al., 2014; Hopper et al., 2014; Rychert et al., 2018; Rychert et al., 2013).

In contrast to many tectonically active regions with elevated mantle geotherms where a large Sp arrival is observed from the base of the lithosphere (e.g. Fischer et al., 2010; Hansen et al., 2015; Hopper & Fischer, 2018), in Anatolia a strong and ubiquitous phase from the LAB depth range is not evident in the Sp CCP stack obtained with the 4-100 s bandpass filter. In some locations, weak and vertically localized positive Sp phases representing negative velocity gradients are observed directly beneath the Moho (e.g. ~30°E and 38°E in Figure 11a) but they are absent in other areas (e.g. ~28°E in Figure 11a). However, when we instead applied a 2-20 s bandpass filter before deconvolution, stronger and more continuous LAB phases are observed beneath the Moho across most of the Anatolian region at around 60-90 km depth (Figures 16a, S6 & S7). This depth range approximately corresponds to the top of the low velocity asthenosphere layer (e.g. Figures 13 & S4). This observation of a shallow LAB phase is consistent with the depth of the LAB in Kind et al. (2015), but unlike Kind et al. (2015), we observed the strong LAB phase only at relatively short periods. In addition, the relative amplitude of the LAB phases in this study is low compared to those in Kind et al. (2015), where LAB phase amplitudes are sometimes comparable to Moho phases.

A possible reason for LAB phases to be weak or absent when using 4-100 s filter is that the mantle lithosphere is too thin to be resolved by long wavelength body waves. In other words, the LAB phase is reduced by interference with a larger Moho phase. To test this hypothesis, a numerical experiment was designed with propagator matrix synthetic seismograms. For velocity structures with varying mantle lithospheric thicknesses (Figure 17a), synthetic S waves with the same ray parameter (0.1098 s/km) were recorded by a station at the surface. However, some waves had Gaussian first derivative source time functions with a period of 14 s (~0.07 Hz), while the others had dominant periods of 4 s (0.25 Hz), and bandpass filters of 4-100 s and 2-20 s were applied. Synthetic seismograms were then deconvolved to obtain Sp receiver functions, using the same approach that was applied to the data, and receiver functions were migrated to depth (Figure 17a). When the mantle lithosphere is thinner than 10 km, LAB phases can barely be observed for any filter or dominant period. When mantle lithosphere thickness is more than 10 km but less than 30 km, receiver functions with 4 s source time functions better capture LAB phases with correct depths and stronger amplitudes. When mantle lithosphere thickness is approximately 30 km, 4 s and 14 s receiver functions are similar. These synthetic tests indicate that higher frequency seismograms better resolve LAB phases when mantle lithosphere is thin. When using a 4-100 s bandpass filter with real data, S phases with periods even longer than 14 s are also included, making the LAB even more difficult to observe than in the numerical experiment. The 2-20 s bandpass filter does not significantly alter receiver functions with short-period source time functions compared to the 4-100 s bandpass filter (e.g. middle-right versus middle-left panel in Figure 17a), but it eliminates longer period waveforms that obscure the LAB phase.

However, while the observed LAB phases become more prominent when using 2-20 s filter, the positive velocity gradient phases are relatively weaker with this filter compared to the 4-100 s bandpass (e.g. Figure 16a versus Figure 11a). To better understand this frequency dependence, another synthetic experiment was designed with a similar setup to the former case, but with a lithospheric thickness fixed at 15 km, and a shear velocity increase from 4.0 km/s to 4.4 km/s centered at 120 km depth. The latter is distributed over a depth range as narrow as 10 km and as broad as 45 km (Figure 17b). When a 4-100 s bandpass filter was applied, receiver functions from a 4 s source time functions are more sensitive to the depth range of the velocity increase when the depth range is more than 30 km, while the 14 s receiver functions show less amplitude variation (middle-left versus left-most panel in Figure 17b). However, when a 2-20 s filter was applied, positive velocity gradient phases become much weaker for 4 s receiver functions from velocity gradients broader than 30 km (middle-right versus middle-left panel in Figure 17b). This result is because the long period Green's functions for converted waves originating from the gradual velocity increase are filtered out.

Based on this synthetic test, and the larger amplitude of the observed positive phase from the base of the asthenosphere with the 4-100 s filter relative to the 2-20 s, we conclude that the corresponding positive velocity gradient is likely distributed over a depth extent of at least 30 km. However, if the velocity gradient is distributed over more than 30 km, the synthetics indicate that the amplitude of the phase should continue to increase as the dominant period in the waveforms further increases, for example the 14 s source versus the 4 s source with the 4-100 s filter (middle-left versus left-most panel in Figure 17b). To produce a shift to longer dominant periods, we also performed the CCP stacking with Sp receiver functions from seismograms with a 10-100 s bandpass filter (Figure 16b, S8 & S9). The positive velocity gradient phase in this case is in many places stronger than in the 4-100 s case, especially for profile B-B' (Figure S8a versus Figure 14a), suggesting that the velocity gradient is probably more gradual than a 30 km depth extent.

These synthetic tests show that in order to observe both thin mantle lithosphere and the gradual positive velocity gradient at the base of the low velocity asthenospheric layer, the best choice is to use seismograms with short-period source time functions and filter them with broad bandpass filters (e.g. the cases with a 4 s source time function and a 4-100 s filter in Figure 17). However, with real data, a shorter period filter is often necessary to isolate short period source time function seismograms, and it is key to construct receiver function stacks with different frequency bands to resolve thin layers and velocity gradient depth ranges.

5. Conclusions

A new approach to finding free-surface velocities from the polarizations of P and S arrivals was developed. This approach has the ability to accurately measure the shear velocity from P arrivals and compressional velocity from S arrivals both with synthetic data and real data. With the retrieved free-surface velocities, P and SV components of seismograms are isolated successfully, resulting in clear Sp receiver functions.

Receiver functions were accurately mapped to depth with a novel kernel-based CCP stacking method. Instead of using empirically defined weighting functions or geographic bins, the new method focuses imaging the horizontal discontinuities assumed in CCP stacking using the shape of scattering kernels. Receiver function amplitudes are projected into the stack using weighting functions that highlight locations where the kernel is relatively flat, its depth offset from the conversion point is minimal, and geometric spreading is small. With typical upper mantle seismic velocities, Sp weighting functions span much broader horizontal regions than Ps weighting functions, indicating an advantage for Sp receiver functions when imaging quasi-horizontal structures.

A fast and accurate approach to quantifying the standard deviation of CCP stacking results is derived based on the central limit theorem. The estimated standard deviation requires only one quick calculation, but is very close to the value obtained by bootstrapping after the latter converges over thousands of iterations. The derived expression can be applied to all problems requiring a standard deviation of weighted averages, and it requires neither the sum of weights to be constant nor the weight to be independent of the sample.

Sp receiver function CCP stacking, after careful quality control, resulted in clear images of upper mantle discontinuities beneath the Anatolian region. Using waveforms with periods of 4-100 s, the Moho, the 410-discontinuity, a velocity decrease at depths of 360-380 km, and a prominent positive velocity gradient located between 80 and 150 km depth are observed. The latter positive velocity gradient marks the base of a low velocity asthenospheric layer which appears in numerous prior models of the Anatolian upper mantle. Causes of the pronounced low velocity asthenosphere could be high mantle temperature or the presence of partial melt, which are also indicated by previous geochemical and seismological studies. While the strong positive velocity gradient is observed beneath most of the region, it does not extend far beyond the North Anatolian Fault in western and central-eastern Anatolia, suggesting a relationship between the plate boundary and its hot underlying asthenospheric mantle.

Strong Sp phases from a negative velocity gradient that corresponds to the LAB are not clearly observed in the CCP stack that employed receiver functions with a 4-100 s bandpass filters, but an LAB Sp phase was clearly imaged at 60 to 90 km depth with a 2-20 s filter. Tests with synthetic seismograms show that this frequency dependent behavior is expected with thin mantle lithosphere. This phase is consistent with the upper margin of the low velocity asthenosphere.

Frequency dependence in the amplitude of the Sp phases from the base of the asthenospheric low velocity layer places constraints on the depth extent of its velocity gradient. The Sp phase amplitude is clearly smallest in the CCP stack with the 2-20 s bandpass filter, indicating that the positive velocity gradient occurs over more than 30 km in depth. Beneath much of the region, southern portions of western and central Anatolia in particular, the amplitude of the phase is larger in the CCP stack with a 10-100 s bandpass filter relative to the stack with the 4-100 s bandpass filter, indicating that the depth extent of the velocity gradient is even larger.

Acknowledgements

Seismograms were downloaded either through IRIS Data Management Center BREQ_FAST service or through obspyDMT toolbox (Hosseini & Sigloch, 2017) for data managed by other data centers supporting FDSN Web Services. Waveforms were collected by 11 permanent networks (KO, https://doi.org/10.7914/SN/KO; GE, https://doi.org/10.14470/TR560404; HL, https://doi.org/10.7914/SN/HL; TU; CQ, https://doi.org/10.7914/SN/CQ; HT, https://doi.org/10.7914/SN/HT; GO; HC, https://doi.org/10.7914/SN/HC; MN, https://doi.org/10.13127/SD/fBBBtDtd6q; IU, https://doi.org/10.7914/SN/IU; AB) and 14 temporary networks (YB, https://doi.org/10.7914/SN/YB_2013; YL, https://doi.org/10.7914/SN/YL_2005; YI, https://doi.org/10.15778/RESIF.YI2008; XW, https://doi.org/10.15778/RESIF.XW2007; XY, https://doi.org/10.15778/RESIF.XY2007; Z3, https://doi.org/10.14470/M87550267382; ZZ, https://doi.org/10.14470/MM7557265463; XO; XH, https://doi.org/10.7914/SN/XH_2002; YF; TK; SU; SD). Our thanks to D. Friedman for initial data downloading. Our thanks to A. Fichtner for providing the velocity model of Fichtner et al. (2013) and discussion, and to T. Bakırcı for discussion. Our thanks to Michael Bostock and two anonymous reviewers for their constructive feedback. This work was supported by the U. S. National Science Foundation through awards EAR-1416753 and EAR-1829401.

References

Abgarmi, B., Delph, J. R., Ozacar, A. A., Beck, S. L., Zandt, G., Sandvol, E., et al. (2017). Structure of the crust and African slab beneath the central Anatolian plateau from receiver functions: New insights on isostatic compensation and slab dynamics. *Geosphere, 13*(6), 1774-1787. https://doi.org/10.1130/GES01509.1

Abt, D. L., Fischer, K. M., French, S. W., Ford, H. A., Yuan, H., & Romanowicz, B. (2010). North American lithospheric discontinuity structure imaged by Ps and Sp receiver functions. *Journal of Geophysical Research: Solid Earth, 115*(B9). https://doi.org/10.1029/2009JB006914

Aki, K., & Richards, P. G. (2002). *Quantitative seismology* (2nd ed.): University Science Books.

Angus, D., Wilson, D. C., Sandvol, E., & Ni, J. (2006). Lithospheric structure of the Arabian and Eurasian collision zone in eastern Turkey from S-wave receiver functions. *Geophysical Journal International, 166*(3), 1335-1346. https://doi.org/10.1111/j.1365-246X.2006.03070.x

Bakırcı, T., Yoshizawa, K., & Özer, M. F. (2012). Three-dimensional S-wave structure of the upper mantle beneath Turkey from surface wave tomography. *Geophysical Journal International, 190*(2), 1058-1076. https://doi.org/10.1111/j.1365-246X.2012.05526.x

Berk Biryol, C., Beck, S. L., Zandt, G., & Özacar, A. A. (2011). Segmented African lithosphere beneath the Anatolian region inferred from teleseismic P-wave tomography. *Geophysical Journal International, 184*(3), 1037-1057. https://doi.org/10.1111/j.1365-246X.2010.04910.x

Blom, N., Gokhberg, A., & Fichtner, A. (2020). Seismic waveform tomography of the Central and Eastern Mediterranean upper mantle. *Solid Earth, 11*(2), 669-690. https://doi.org/10.5194/se-11-669-2020

Bostock, M. G., & Rondenay, S. (1999). Migration of scattered teleseismic body waves. *Geophysical Journal International, 137*(3), 732-746. https://doi.org/10.1046/j.1365-246x.1999.00813.x

Bostock, M. G., Rondenay, S., & Shragge, J. (2001). Multiparameter two-dimensional inversion of scattered teleseismic body waves 1. Theory for oblique incidence. *Journal of Geophysical Research Solid Earth, 106*(B12), 30771-30782. https://doi.org/10.1029/2001JB000330

Crameri, F. (2018). Geodynamic diagnostics, scientific visualisation and StagLab 3.0. *Geoscientific Model Development, 11*(6), 2541-2562. https://doi.org/10.5194/gmd-11-2541-2018

Delph, J. R., Biryol, C. B., Beck, S. L., Zandt, G., & Ward, K. M. (2015). Shear wave velocity structure of the Anatolian Plate: anomalously slow crust in southwestern Turkey. *Geophysical Journal International, 202*(1), 261-276. https://doi.org/10.1093/gji/ggv141

Dueker, K. G., & Sheehan, A. F. (1997). Mantle discontinuity structure from midpoint stacks of converted P to S waves across the Yellowstone hotspot track. *Journal of Geophysical Research: Solid Earth, 102*(B4), 8313-8327.

Faccenna, C., Bellier, O., Martinod, J., Piromallo, C., & Regard, V. (2006). Slab detachment beneath eastern Anatolia: A possible cause for the formation of the North Anatolian fault. *Earth and Planetary Science Letters, 242*(1-2), 85-97. https://doi.org/10.1016/j.epsl.2005.11.046

Farra, V., & Vinnik, L. (2000). Upper mantle stratification by P and S receiver functions. *Geophysical Journal International, 141*(3), 699-712. https://doi.org/10.1046/j.1365-246x.2000.00118.x

Fichtner, A., Saygin, E., Taymaz, T., Cupillard, P., Capdeville, Y., & Trampert, J. (2013). The deep structure of the North Anatolian Fault Zone. *Earth and Planetary Science Letters, 373*, 109-117. https://doi.org/10.1016/j.epsl.2013.04.027

Fischer, K. M., Ford, H. A., Abt, D. L., & Rychert, C. A. (2010). The lithosphere-asthenosphere boundary. *Annual Review of Earth and Planetary Sciences, 38*, 551-575. https://doi.org/10.1146/annurev-earth-040809-152438

Ford, H. A., Fischer, K. M., & Lekic, V. (2014). Localized shear in the deep lithosphere beneath the San Andreas fault system. *Geology, 42*(4), 295-298. https://doi.org/10.1130/G35128.1

Frederiksen, A. W., Thompson, D. A., Rost, S., Cornwell, D. G., Gülen, L., Houseman, G. A., et al. (2015). Crustal thickness variations and isostatic disequilibrium across the North Anatolian Fault, western Turkey. *Geophysical Research Letters, 42*(3), 751-757. https://doi.org/10.1002/2014GL062401

Gans, C. R., Beck, S. L., Zandt, G., Biryol, C. B., & Ozacar, A. A. (2009). Detecting the limit of slab break-off in central Turkey: new high-resolution Pn tomography results. *Geophysical Journal International, 179*(3), 1566-1572. https://doi.org/10.1111/j.1365-246X.2009.04389.x

Gök, R., Sandvol, E., Türkelli, N., Seber, D., & Barazangi, M. (2003). Sn attenuation in the Anatolian and Iranian plateau and surrounding regions. *Geophysical Research Letters, 30*(24). https://doi.org/10.1029/2003GL018020

Govers, R., & Fichtner, A. (2016). Signature of slab fragmentation beneath Anatolia from full-waveform tomography. *Earth and Planetary Science Letters, 450*, 10-19. https://doi.org/10.1016/j.epsl.2016.06.014

Hannemann, K., Krüger, F., Dahm, T., & Lange, D. (2016). Oceanic lithospheric S-wave velocities from the analysis of P-wave polarization at the ocean floor. *Geophysical Supplements to the Monthly Notices of the Royal Astronomical Society, 207*(3), 1796-1817. https://doi.org/10.1093/gji/ggw342

Hansen, S. M., Dueker, K., & Schmandt, B. (2015). Thermal classification of lithospheric discontinuities beneath USArray. *Earth and Planetary Science Letters, 431*, 36-47. https://doi.org/10.1016/j.epsl.2015.09.009

Hansen, S. M., & Schmandt, B. (2017). P and S wave receiver function imaging of subduction with scattering kernels. *Geochemistry, Geophysics, Geosystems, 18*(12), 4487-4502. https://doi.org/10.1002/2017GC007120

Hopper, E., & Fischer, K. M. (2018). The changing face of the lithosphere-asthenosphere boundary: Imaging continental scale patterns in upper mantle structure across the contiguous US with Sp converted waves. *Geochemistry, Geophysics, Geosystems, 19*(8), 2593-2614. https://doi.org/10.1029/2018GC007476

Hopper, E., Ford, H. A., Fischer, K. M., Lekic, V., & Fouch, M. J. (2014). The lithosphere–asthenosphere boundary and the tectonic and magmatic history of the northwestern United States. *Earth and Planetary Science Letters, 402*, 69-81. https://doi.org/10.1016/j.epsl.2013.12.016

Hosseini, K., & Sigloch, K. (2017). obspyDMT: a Python toolbox for retrieving and processing of large seismological datasets. *Solid Earth, 8*. https://doi.org/10.5194/se-8-1047-2017

Hua, J., Fischer, K. M., Mancinelli, N. J., & Bao, T. (2020). Imaging with pre-stack migration based on Sp scattering kernels. *Geophysical Journal International, 220*(1), 428-449. https://doi.org/10.1093/gji/ggz459

Hua, J., Fischer, K. M., & Savage, M. K. (2018). The lithosphere–asthenosphere boundary beneath the South Island of New Zealand. *Earth and Planetary Science Letters, 484*, 92-102. https://doi.org/10.1016/j.epsl.2017.12.011

Jolivet, L., Faccenna, C., Huet, B., Labrousse, L., Le Pourhiet, L., Lacombe, O., et al. (2013). Aegean tectonics: Strain localisation, slab tearing and trench retreat. *Tectonophysics, 597-598*, 1-33. https://doi.org/10.1016/j.tecto.2012.06.011

Kandilli Observatory and Earthquake Research Institute Bosphorus Univ. (2001). *Bogazici University Kandilli Observatory And Earthquake Research Institute*. International Federation of Digital Seismograph Networks. Dataset/Seismic Network.

Karabulut, H., Paul, A., Özbakır, A. D., Ergün, T., & Şentürk, S. (2019). A new crustal model of the Anatolia–Aegean domain: evidence for the dominant role of isostasy in the support of the Anatolian plateau. *Geophysical Journal International, 218*(1), 57-73. https://doi.org/10.1093/gji/ggz147

Keith, C. M., & Crampin, S. (1977). Seismic body waves in anisotropic media: synthetic seismograms. *Geophysical Journal International, 49*(1), 225-243.

Kennett, B. L. (1991). The removal of free surface interactions from three-component seismograms. *Geophysical Journal International, 104*(1), 153-154. https://doi.org/10.1111/j.1365-246X.1991.tb02501.x

Kennett, B. L., Engdahl, E., & Buland, R. (1995). Constraints on seismic velocities in the Earth from traveltimes. *Geophysical Journal International, 122*(1), 108-124. https://doi.org/10.1111/j.1365-246X.1995.tb03540.x

Keskin, M. (2003). Magma generation by slab steepening and breakoff beneath a subduction-accretion complex: An alternative model for collision-related volcanism in Eastern Anatolia, Turkey. *Geophysical Research Letters, 30*(24). https://doi.org/10.1029/2003GL018019

Kind, R., Eken, T., Tilmann, F., Sodoudi, F., Taymaz, T., Bulut, F., et al. (2015). Thickness of the lithosphere beneath Turkey and surroundings from S-receiver functions. *Solid Earth, 6*(3), 971-984. https://doi.org/10.5194/se-6-971-2015

Kind, R., Yuan, X., & Kumar, P. (2012). Seismic receiver functions and the lithosphere–asthenosphere boundary. *Tectonophysics, 536*, 25-43. https://doi.org/10.1016/j.tecto.2012.03.005

Lekić, V., & Fischer, K. M. (2014). Contrasting lithospheric signatures across the western United States revealed by Sp receiver functions. *Earth and Planetary Science Letters, 402*, 90-98. https://doi.org/10.1016/j.epsl.2013.11.026

Lekić, V., & Fischer, K. M. (2017). Interpreting spatially stacked Sp receiver functions. *Geophysical Journal International, 210*(2), 874-886. https://doi.org/10.1093/gji/ggx206

Lekic, V., French, S. W., & Fischer, K. M. (2011). Lithospheric thinning beneath rifted regions of southern California. *Science, 334*(6057), 783-787. https://doi.org/10.1126/science.1208898

Licciardi, A., Eken, T., Taymaz, T., Agostinetti, N. P., & Yolsal-Çevikbilen, S. (2018). Seismic anisotropy in central North Anatolian Fault Zone and its implications on crustal deformation. *Physics of the Earth and Planetary Interiors, 277*, 99-112. https://doi.org/10.1016/j.pepi.2018.01.012

Ligorria, J. P., & Ammon, C. J. (1999). Iterative deconvolution and receiver-function estimation. *Bulletin of the seismological Society of America, 89*(5), 1395-1400.

Mancinelli, N., & Fischer, K. (2017). The spatial sensitivity of Sp converted waves—scattered-wave kernels and their applications to receiver-function migration and inversion. *Geophysical Journal International, 212*(3), 1722-1735. https://doi.org/10.1093/gji/ggx506

McNab, F., Ball, P. W., Hoggard, M. J., & White, N. J. (2018). Neogene Uplift and Magmatism of Anatolia: Insights From Drainage Analysis and Basaltic Geochemistry. *Geochemistry, Geophysics, Geosystems, 19*(1), 175-213. https://doi.org/10.1002/2017GC007251

Mutlu, A. K., & Karabulut, H. (2011). Anisotropic Pn tomography of Turkey and adjacent regions. *Geophysical Journal International, 187*(3), 1743-1758. 10.1111/j.1365-246X.2011.05235.x

Nikogosian, I., Gartner, A. B., van Bergen, M., Mason, P., & Van Hinsbergen, D. J. (2018). Mantle sources of recent Anatolian intraplate magmatism: A regional plume or local tectonic origin? *Tectonics, 37*(12), 4535-4566. https://doi.org/10.1029/2018TC005219

Ozacar, A. A., Gilbert, H., & Zandt, G. (2008). Upper mantle discontinuity structure beneath East Anatolian Plateau (Turkey) from receiver functions. *Earth and Planetary Science Letters, 269*(3-4), 427-435. https://doi.org/10.1016/j.epsl.2008.02.036

Park, S., & Ishii, M. (2018). Near-surface compressional and shear wave speeds constrained by body-wave polarization analysis. *Geophysical Journal International, 213*(3), 1559-1571. https://doi.org/10.1093/gji/ggy072

Park, S., Tsai, V. C., & Ishii, M. (2019). Frequency-Dependent P Wave Polarization and Its Subwavelength Near-Surface Depth Sensitivity. *Geophysical Research Letters*. https://doi.org/10.1029/2019GL084892

Portner, D. E., Delph, J. R., Biryol, C. B., Beck, S. L., Zandt, G., Özacar, A. A., et al. (2018). Subduction termination through progressive slab deformation across Eastern Mediterranean subduction zones from updated P-wave tomography beneath Anatolia. *Geosphere, 14*(3), 907-925. https://doi.org/10.1130/GES01617.1

Reid, M. R., Schleiffarth, W. K., Cosca, M. A., Delph, J. R., Blichert-Toft, J., & Cooper, K. M. (2017). Shallow melting of MORB-like mantle under hot continental lithosphere, Central Anatolia. *Geochemistry, Geophysics, Geosystems, 18*(5), 1866-1888. https://doi.org/10.1002/2016GC006772

Reilinger, R., McClusky, S., Vernant, P., Lawrence, S., Ergintav, S., Cakmak, R., et al. (2006). GPS constraints on continental deformation in the Africa-Arabia-Eurasia continental collision zone and implications for the dynamics of plate interactions. *Journal of Geophysical Research: Solid Earth, 111*(B5). https://doi.org/10.1029/2005JB004051

Rondenay, S. (2009). Upper mantle imaging with array recordings of converted and scattered teleseismic waves. *Surveys in Geophysics, 30*(4-5), 377-405. https://doi.org/10.1007/s10712-009-9071-5

Rondenay, S., Bostock, M. G., & Fischer, K. M. (2005). Multichannel inversion of scattered teleseismic body waves: Practical considerations and applicability. *Washington Dc American Geophysical Union Geophysical Monograph, 157*, 187-203. https://doi.org/10.1029/157GM12

Rychert, C. A., Harmon, N., & Tharimena, S. (2018). Scattered wave imaging of the oceanic plate in Cascadia. *Science advances, 4*(2), eaao1908. https://doi.org/10.1126/sciadv.aao1908

Rychert, C. A., Laske, G., Harmon, N., & Shearer, P. M. (2013). Seismic imaging of melt in a displaced Hawaiian plume. *Nature Geoscience, 6*(8), 657-660. https://doi.org/10.1038/ngeo1878

Salaün, G., Pedersen, H. A., Paul, A., Farra, V., Karabulut, H., Hatzfeld, D., et al. (2012). High-resolution surface wave tomography beneath the Aegean-Anatolia region: constraints on upper-mantle structure. *Geophysical Journal International, 190*(1), 406-420. https://doi.org/10.1111/j.1365-246X.2012.05483.x

Schildgen, T. F., Yıldırım, C., Cosentino, D., & Strecker, M. R. (2014). Linking slab break-off, Hellenic trench retreat, and uplift of the Central and Eastern Anatolian plateaus. *Earth-Science Reviews, 128*, 147-168. https://doi.org/10.1016/j.earscirev.2013.11.006

Şengör, A., Özeren, S., Genç, T., & Zor, E. (2003). East Anatolian high plateau as a mantle-supported, north-south shortened domal structure. *Geophysical Research Letters, 30*(24). https://doi.org/10.1029/2003GL017858

Şengör, A. M. C., Özeren, M. S., Keskin, M., Sakınç, M., Özbakır, A. D., & Kayan, İ. (2008). Eastern Turkish high plateau as a small Turkic-type orogen: Implications for post-collisional crust-forming processes in Turkic-type orogens. *Earth-Science Reviews, 90*(1-2), 1-48. https://doi.org/10.1016/j.earscirev.2008.05.002

Svenningsen, L., & Jacobsen, B. (2007). Absolute S-velocity estimation from receiver functions. *Geophysical Journal International, 170*(3), 1089-1094. https://doi.org/10.1111/j.1365-246X.2006.03505.x

Vanacore, E. A., Taymaz, T., & Saygin, E. (2013). Moho structure of the Anatolian Plate from receiver function analysis. *Geophysical Journal International, 193*(1), 329-337. https://doi.org/10.1093/gji/ggs107

Vinnik, L., & Farra, V. (2002). Subcratonic low-velocity layer and flood basalts. *Geophysical Research Letters, 29*(4), 8-1-8-4. https://doi.org/10.1029/2001GL014064

Wei, W., Zhao, D., Wei, F., Bai, X., & Xu, J. (2019). Mantle Dynamics of the Eastern Mediterranean and Middle East: Constraints From P-Wave Anisotropic Tomography. *Geochemistry, Geophysics, Geosystems, 20*(10), 4505-4530. https://doi.org/10.1029/2019GC008512

Wiechert, E., & Zoeppritz, K. (1907). Über erdbebenwellen. *Nachrichten von der Gesellschaft der Wissenschaften zu Göttingen, Mathematisch-Physikalische Klasse, 1907*, 415-549.

Wittlinger, G., & Farra, V. (2007). Converted waves reveal a thick and layered tectosphere beneath the Kalahari super-craton. *Earth and Planetary Science Letters, 254*(3-4), 404-415. https://doi.org/10.1016/j.epsl.2006.11.048

Yuan, X., Kind, R., Li, X., & Wang, R. (2006). The S receiver functions: synthetics and data example. *Geophysical Journal International, 165*(2), 555-564. https://doi.org/10.1111/j.1365-246X.2006.02885.x

Zhang, H., & Schmandt, B. (2019). Application of Ps Scattering Kernels to Imaging the Mantle Transition Zone with Receiver Functions. *Journal of Geophysical Research: Solid Earth*. https://doi.org/10.1029/2018JB016274

Zhu, H. (2018). High Vp/Vs ratio in the crust and uppermost mantle beneath volcanoes in the Central and Eastern Anatolia. *Geophysical Journal International, 214*(3), 2151-2163. https://doi.org/10.1093/gji/ggy253

Zhu, L., Mitchell, B. J., Akyol, N., Cemen, I., & Kekovali, K. (2006). Crustal thickness variations in the Aegean region and implications for the extension of continental crust. *Journal of Geophysical Research: Solid Earth, 111*(B1). https://doi.org/10.1029/2005JB003770

Zor, E., Sandvol, E., Gürbüz, C., Türkelli, N., Seber, D., & Barazangi, M. (2003). The crustal structure of the East Anatolian plateau (Turkey) from receiver functions. *Geophysical Research Letters, 30*(24). https://doi.org/10.1029/2003GL018192

Figures:

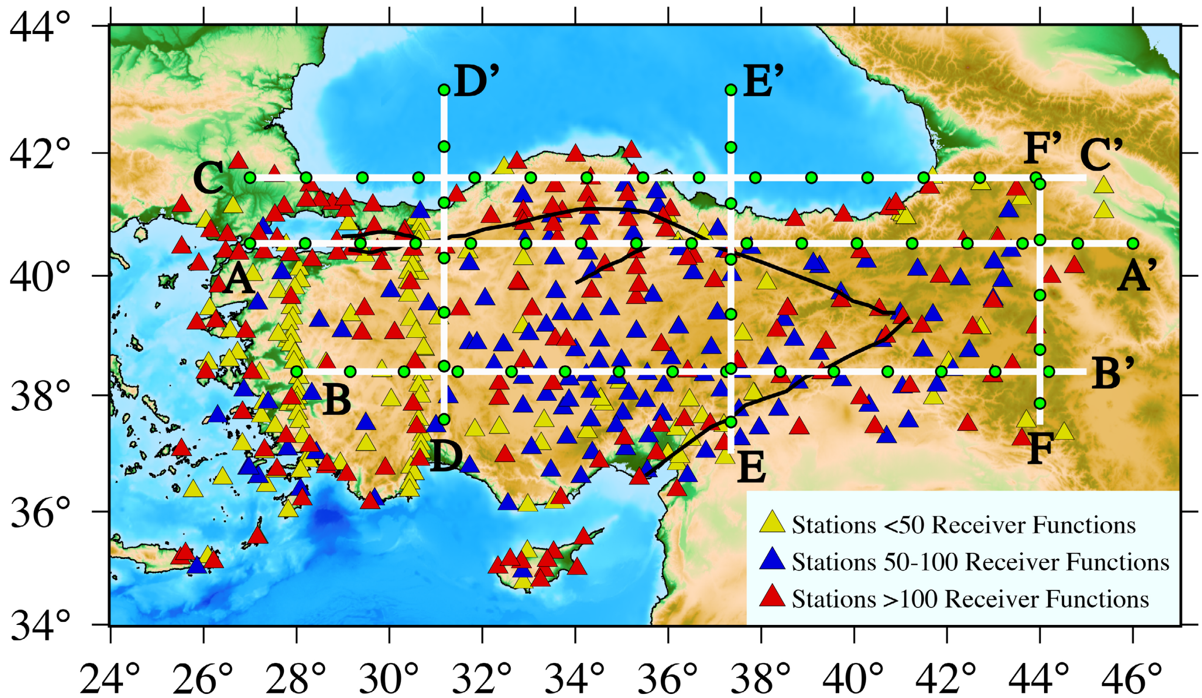

Figure 1. Map of the study region covering the Anatolian Plate. Broadband stations employed in this study are triangles; stations with less than 50 Sp receiver functions are shown in yellow color, those with 50 to 100 receiver functions are in blue, and those with more than 100 receiver functions are in red. The North Anatolian Fault and East Anatolian Fault are shown by black lines. Bold white are the locations of profiles discussed in this paper; the distance between the green circles is 100 km.

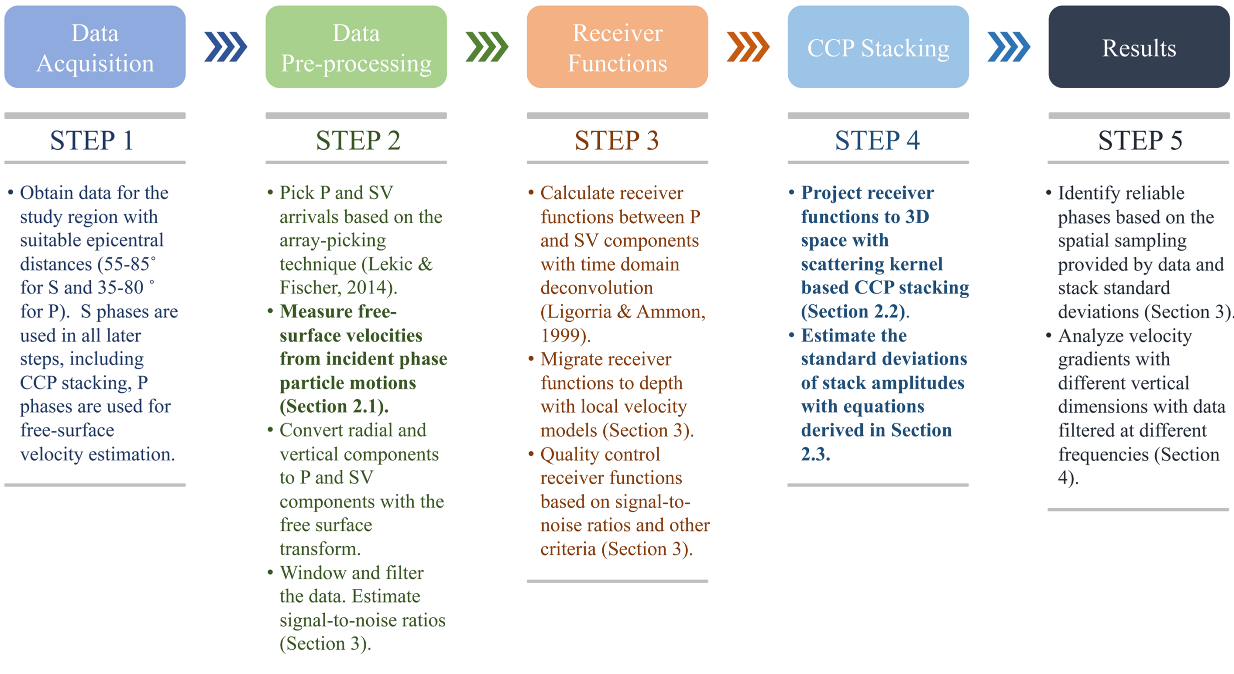

Figure 2. Flow chart with the five main steps involved in calculating the Sp CCP stack. Operations shown in bold correspond to methodological improvements introduced in this study.

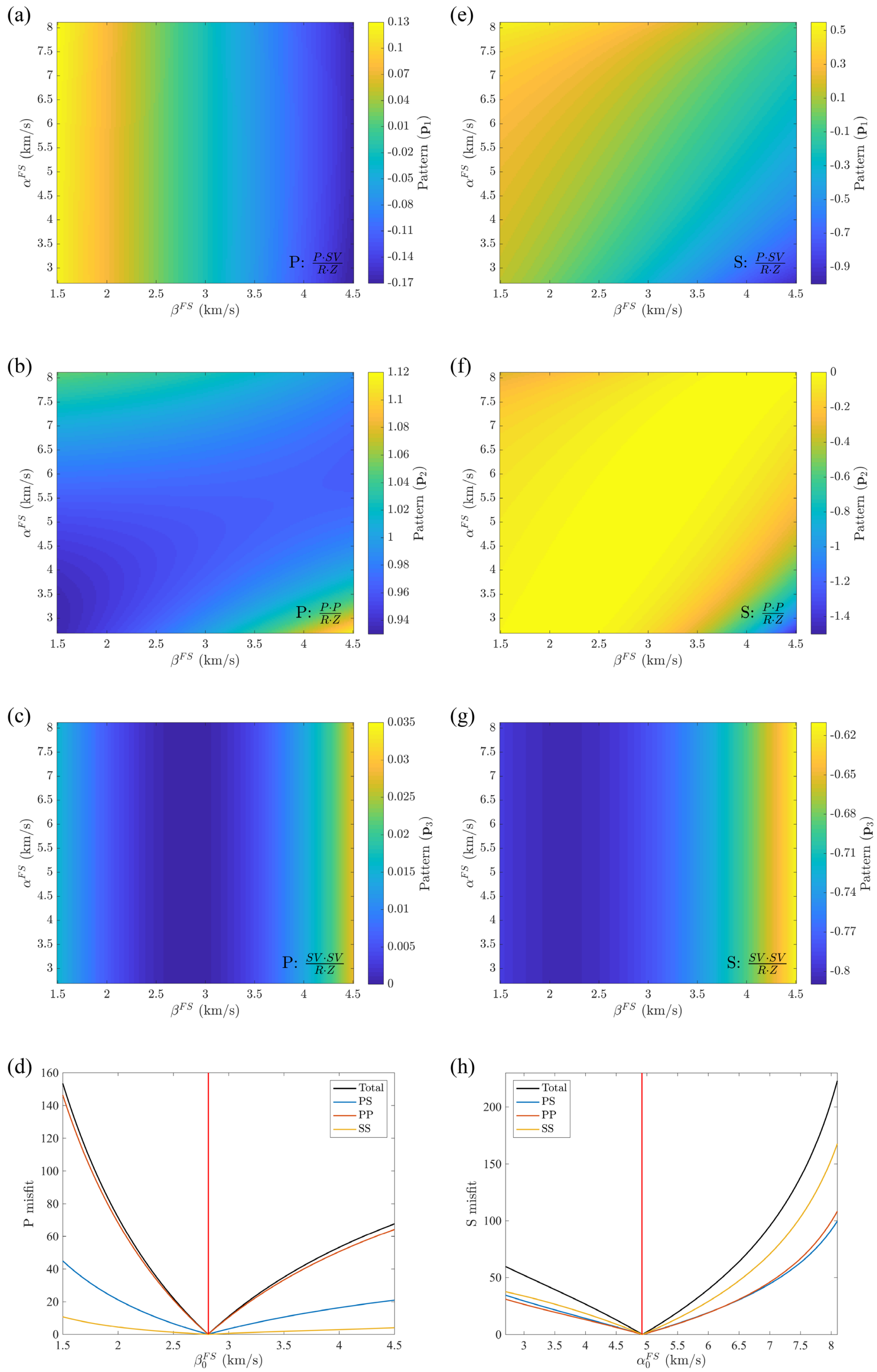

Figure 3. Particle motion patterns in equation (4) obtained with synthetic seismograms generated for a half space with V_p=4.92 km/s and V_s=2.82 km/s. (a) The pattern $\mathbf{C}_1$ in equation (4) for a P arrival with a ray parameter of 0.0482 s/km. Colors show the value of the pattern for varying α^{FS} and β^{FS}. The label at the bottom right corner indicates the arrival phase and the equation for the pattern. (b)-(c) similar to (a), but for $\mathbf{C}_2$ and $\mathbf{C}_3$. (d) Determination of β_0^{FS} by

minimizing the misfit function defined in section 2.1. The black curve shows the value of the total misfit function defined in equation (6) for different β_0^{FS}, the blue curve shows the value when the misfit function is defined as $\left\|\mathbf{C}_1 - \mathbf{C}_1^p\right\|_2$, the red curve is for misfit function $\left\|\mathbf{C}_2 - \mathbf{C}_2^p\right\|_2$, and the yellow curve is for misfit function $\left\|\mathbf{C}_3 - \mathbf{C}_3^p\right\|_2$. $\mathbf{C}_2$ makes the largest contribution to the total misfit. The vertical red line shows the true β_0^{FS} from the structure used to calculate the synthetic waveforms. (e)-(g) similar to (a)-(c) but for an S-arrival with a ray parameter of 0.1098 s/km. (h) similar to (d) but searching for α_0^{FS}; the vertical red line indicates the true α_0^{FS}.

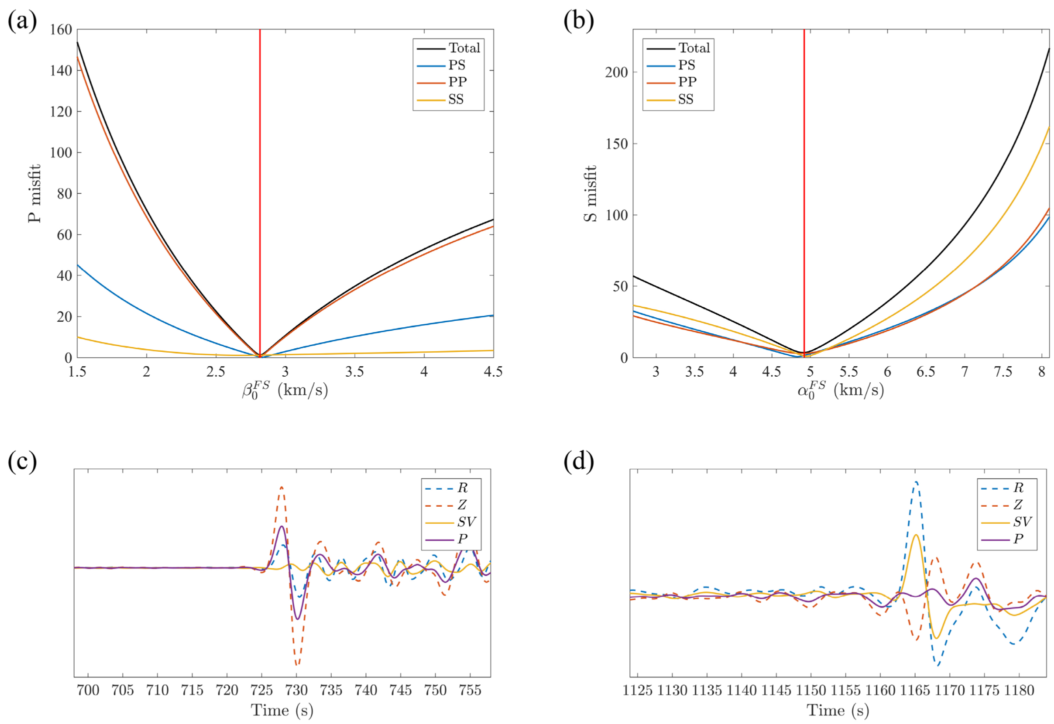

Figure 4. (a) Plot similar to Figure 3d and (b) plot similar to Figure 3h but using records from two real events. Both the P arrival event and the S arrival event have the same ray parameters as those used in the synthetic case in Figure 3. Colors and curves are defined identically to those in Figure 3. The only difference is the vertical red lines show the β_0^{FS} and α_0^{FS} values obtained by minimizing the misfit function in equation (6); their values are equal to the half space velocities used in Figure 3. (c) P and SV component example for the real P arrival used in (a). The x-axis is time from the earthquake origin time. Blue and red dashed lines show the radial and vertical components of the seismogram, and yellow and purple lines are the P and SV components based on equation (1) and the determined β_s^{FS} and α_s^{FS} values. (d) Similar to (c), but for the real S arrival used in (b).

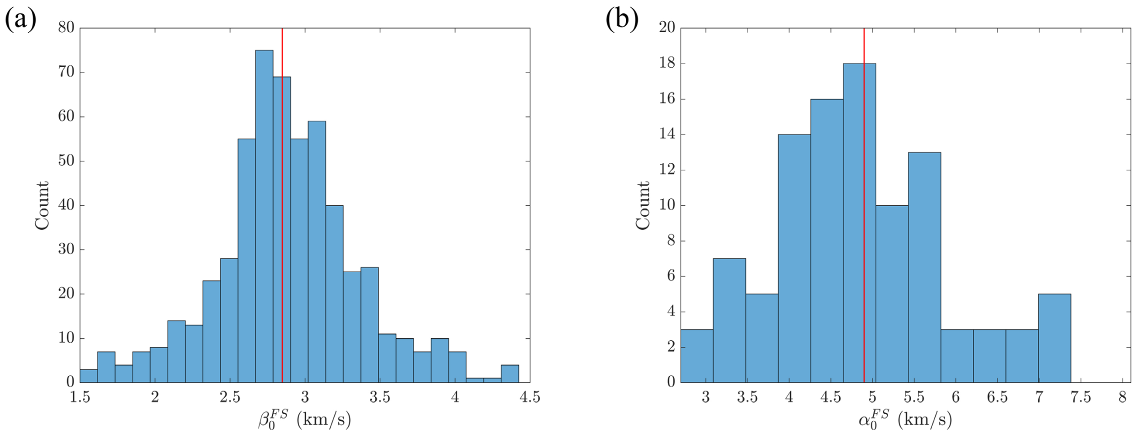

Figure 5. (a) Histogram of β_0^{FS} values obtained from 562 individual P-arrivals whose weight for free surface velocity calculation is not zero. The bin width is 0.117 km/s. The red line shows the final determined β_s^{FS} from the weighted average of individual β_0^{FS}. (b) Similar to (a) but with results for α_0^{FS} from 100 individual S-arrivals. The bin width is 0.39 km/s.

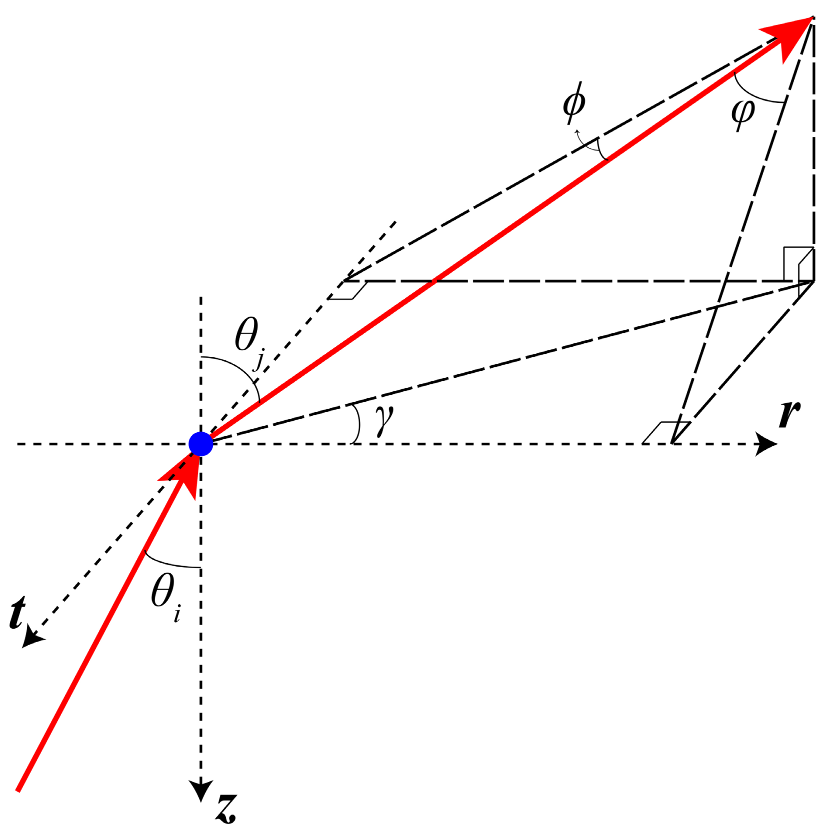

Figure 6. Schematic plot of the scattering process. Ray paths of the incident wave propagating in the *r*-*z* plane and the scattered wave are shown by red lines. The scatterer is marked by the blue dot. The coordinates and angles used for calculating the phase delay time isochron slope angle are also labelled.

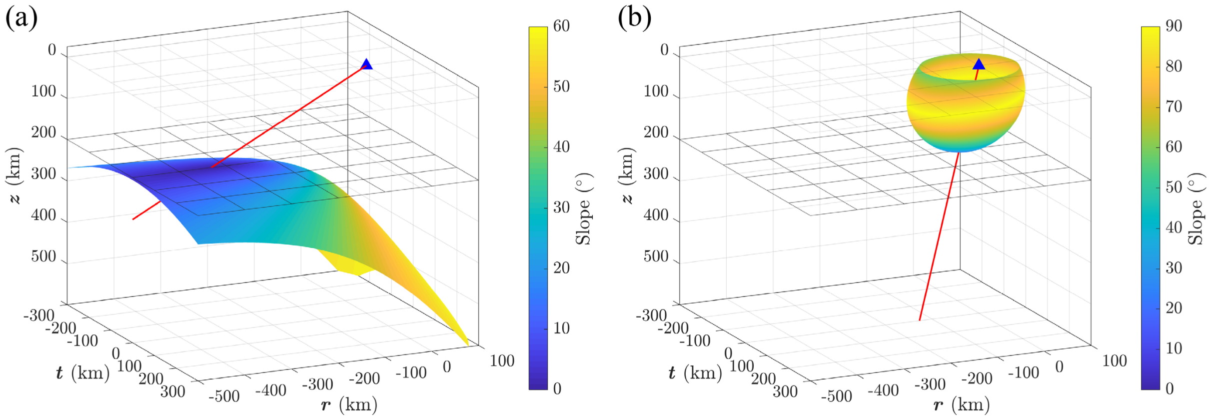

Figure 7. Examples of converted phase delay time isochrons (curved surfaces) for Sp (a) and Ps (b) phases. This case is for a half space with V_p=7.8 km/s and V_s=4.3 km/s. Conversion points are at 200 km depth and ray paths are shown by red lines. The station is a blue triangle at (0 km, 0 km, 0 km). The black mesh at 200 km depth shows the horizontal plane for CCP stacking. (a) The isochron for Sp scattering, with an incident S wave ray parameter of 0.1098 s/km. Delay time for the isochron is -27.76 s. Colors on the isochron are the slope angle calculated from equation (12). (b) Similar to (a) but for Ps scattering, and an incident P wave ray parameter of 0.0482 s/km. Delay time for the isochron is 21.74 s

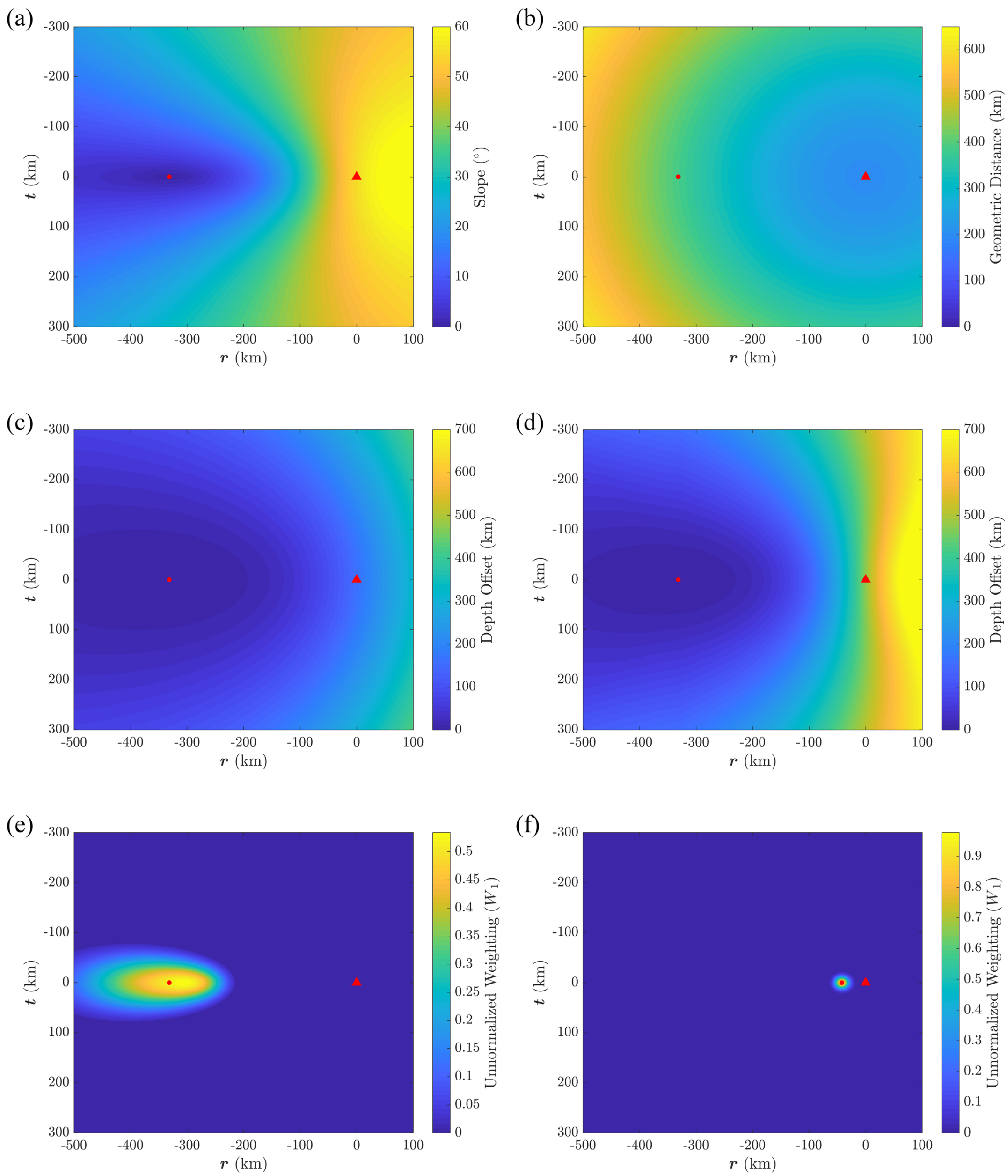

Figure 8. Properties related to the weighting function in equation (16) calculated for the same structure as used in Figure 7. (a)-(e) correspond to the Sp scattering case in Figure 7a and are for a depth of 200 km. The red circle shows the conversion point, and the triangle shows the horizontal position of the station projected downward from the surface. (a) The slope angle distribution based on equation (12). (b) The geometric distance from each point to the station. (c) The depth offset from the isochron to the stacking depth at 200 km (black mesh in Figure 7a). (d) The depth offset estimated based equation (15) which is comparable to the true depth offset in (c) near the conversion point. (e) The complete weighting function based on equation (16) that combines information in (a), (b) and (d); (f) Similar to (e), but for the Ps scattering case in Figure 7b.

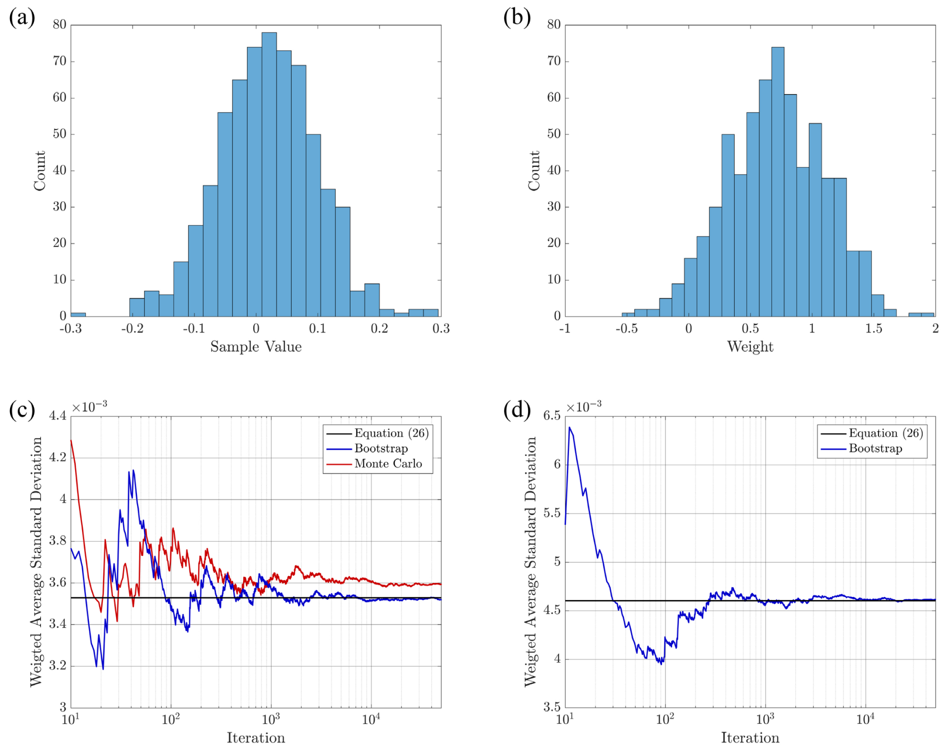

Figure 9. (a) Histogram of 648 randomly generated samples from a normal distribution of $N(0.02, 0.08^2)$, and the bin width is 0.024. (b) Histogram of 648 randomly generated weights from a normal distribution of $N(0.7, 0.4^2)$, and the bin width is 0.101. (c) The standard deviation of the weighted average of the samples in (a) with weights in (b). The black line shows the standard deviation estimate from equation (26); the blue line shows the standard deviation estimate from bootstrapping, where the x-axis shows the number of bootstrap iterations; the red line shows the true standard deviation estimated from a Monte Carlo approach, where the x-axis shows the number of Monte Carlo simulations. (d) The standard deviation of the CCP stack of Anatolia receiver function amplitudes at 40.5°N, 38°E and 125 km depth; the lines have the same meaning as in (c).

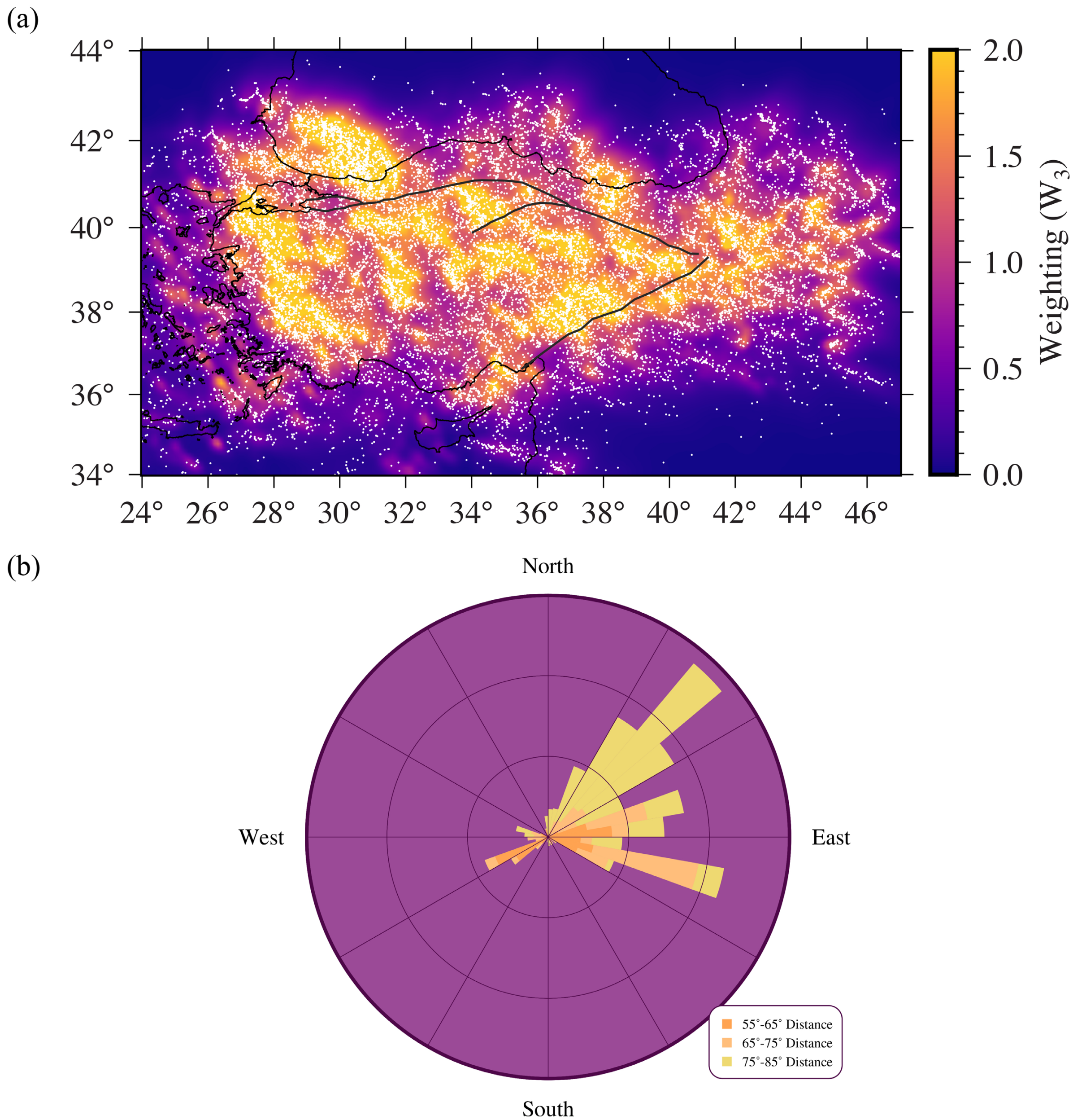

Figure 10. (a) Sp receiver function data sampling of the Anatolian region. Color shows the combined receiver function weights, W_3 (equation 27), at 125 km depth. Locations with W_3 values of more than 2.0 are shown by the yellow color that corresponds to 2.0 on the scale. White dots are piercing point locations of the 23,787 converted P wave ray paths employed in the final CCP stack. The weighting is generally stronger where piercing points are denser. (b) Back-azimuth and epicentral distance distribution for the 23,787 records. The diagram is divided into 10° back-azimuthal bins. Radial lines measure the percentage of the data that falls within a back-azimuthal bin. The maximum radius corresponds to 15%, and thin black circles mark 5% and 10%. In each back-azimuthal bin, lengths of sectors with different colors represent the proportion of earthquakes with different epicentral distance ranges as specified by the legend.

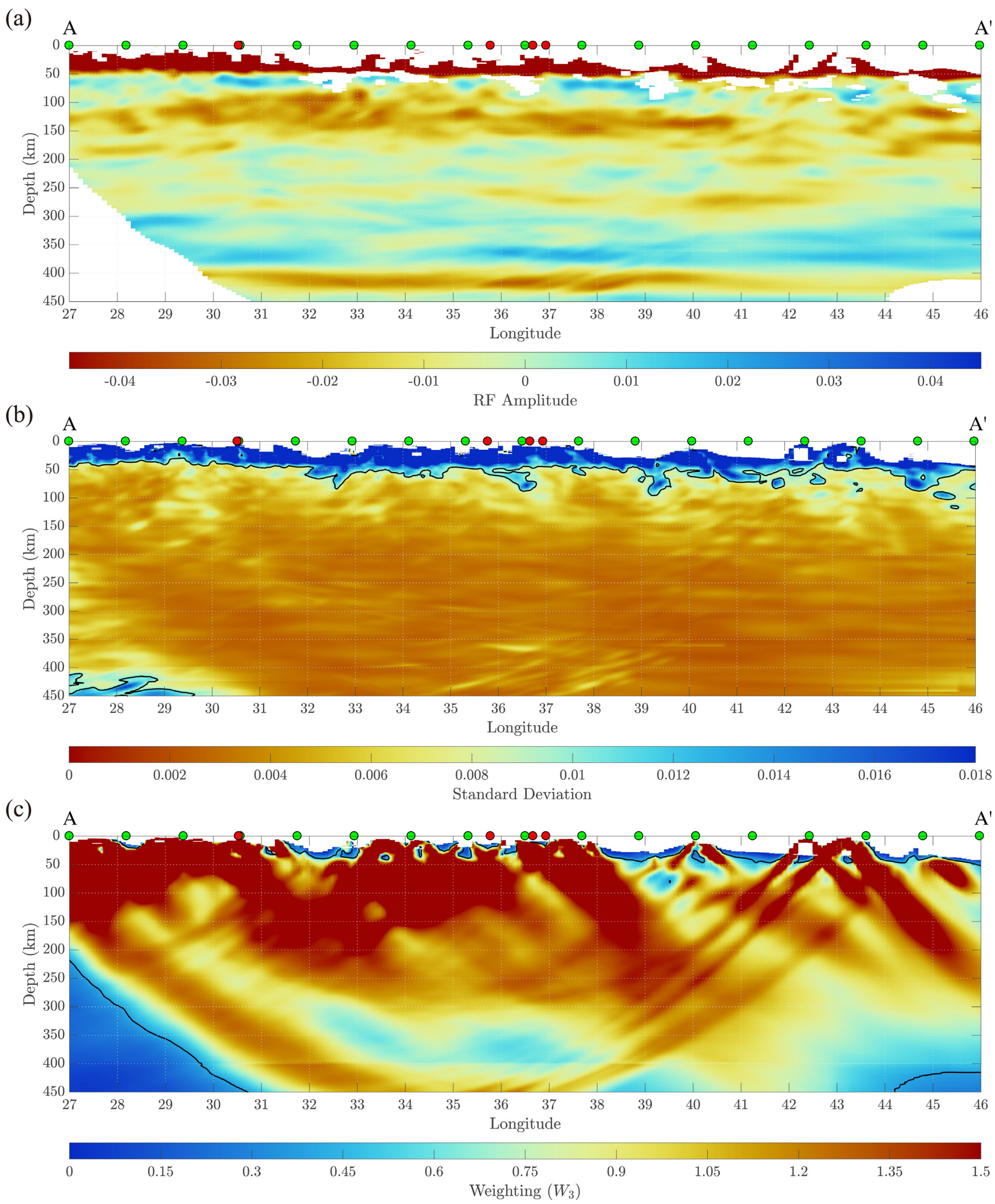

Figure 11. Properties of the Sp CCP stack shown on east-west oriented profile A-A' at 40.5°N. Horizontal axes are annotated with longitude, and vertical axes are annotated with depth. The location of the profile is shown in Figure 1. Green circles at the top of the profiles correspond to green circles on the map, with 100 km distance between them. Red circles show the intersection point of the profile with the North Anatolian Fault or East Anatolian Fault. The length of the profile is 1,603 km. (a) Sp CCP stack amplitude. Red amplitudes correspond to negative Sp phases and a velocity increase with depth (e.g. the Moho above 50 km and the 410-discontinuity); blue amplitudes correspond to positive Sp phases and a velocity decrease with depth. Phases with amplitude exceeding the limit of the color bar are shown by the boundary color (e.g. the Moho phase). Blank areas indicate zones where the image is not robust and should not be interpreted, either due to a standard deviation that exceeds both 0.01 and half of the

receiver function amplitude, or due to a weight value W_3 (equation 27) that is less than 0.4. (b) The standard deviation of the Sp CCP stack amplitude from equation (26). Black line shows the contour where standard deviation equals 0.01. c) The total weight W_3. Black line shows the contour where equals 0.4. Locations with W_3 that is more than the limit of the color bar are shown by the maximum color. The color map used in this figure and all others with CCP stacks is from Crameri (2018) although with a 50% increased saturation.

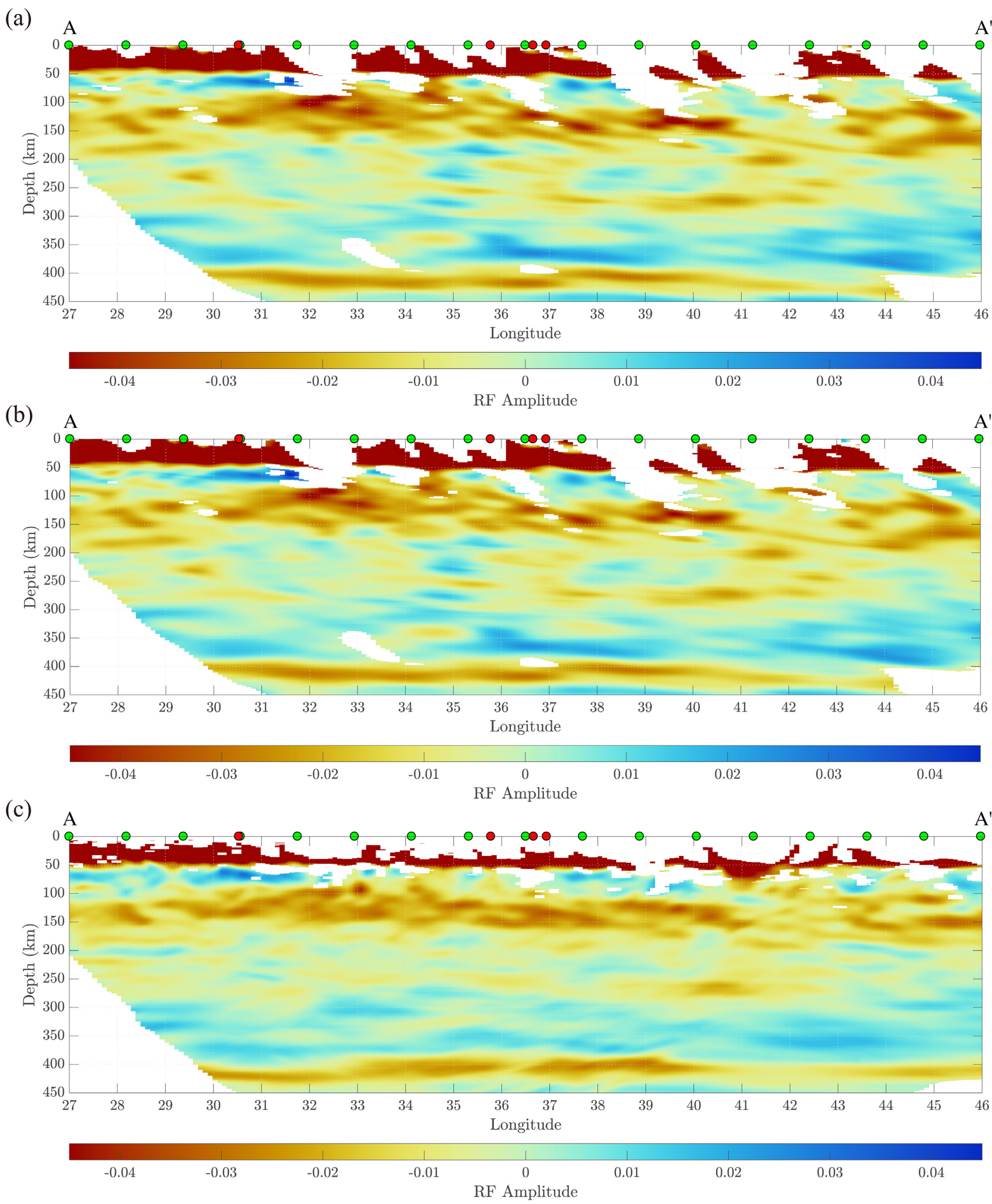

Figure 12. Sp CCP stack amplitudes on profile A-A' using different methods and velocity structures. Symbols and notations identical to Figure 11a. (a) CCP stack obtained using the empirical weighting function defined by a 13 s P wave Fresnel Zone (Lekic et al., 2011). Because the weighting function is defined differently than in Figure 11a, locations with W_3 less than 40 are blank, while the criteria for standard deviation are the same. (b) CCP stack using the free-surface velocity determination method in Abt et al. (2010), and the stacking method as in (a). Blank regions are identified identically to (a). (c) CCP stack using the methods also used in Figure 11a, except with the full-waveform inversion model of Fichtner et al. (2013). Blank regions are identified identically to Figure 11a.

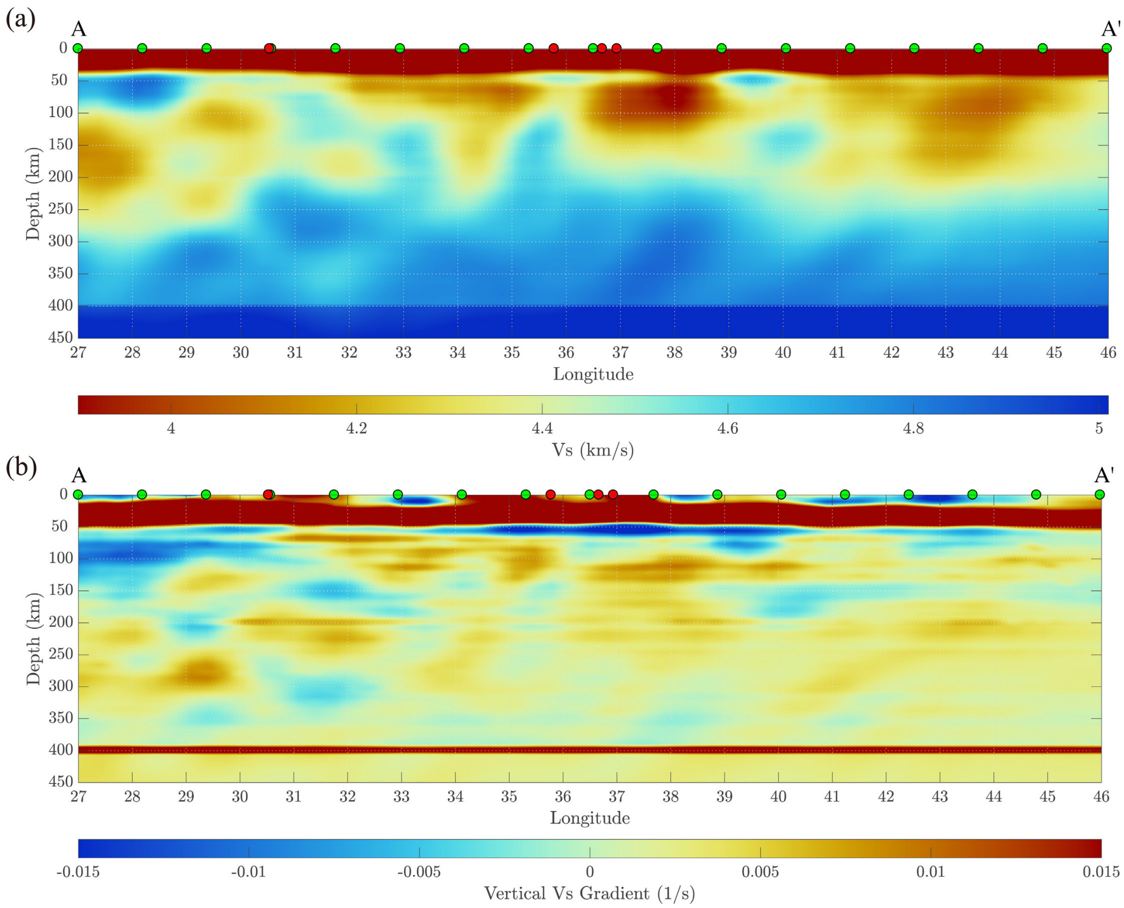

Figure 13. Shear velocity model on profile A-A’. (a) Shear wave velocity from Blom et al. (2020). Velocities exceeding the limit of the color bar are shown by the color at the limit (e.g. crustal velocities). (b) Vertical gradients in shear-wave velocity from Blom et al. (2020) smoothed over a 5 km depth window.

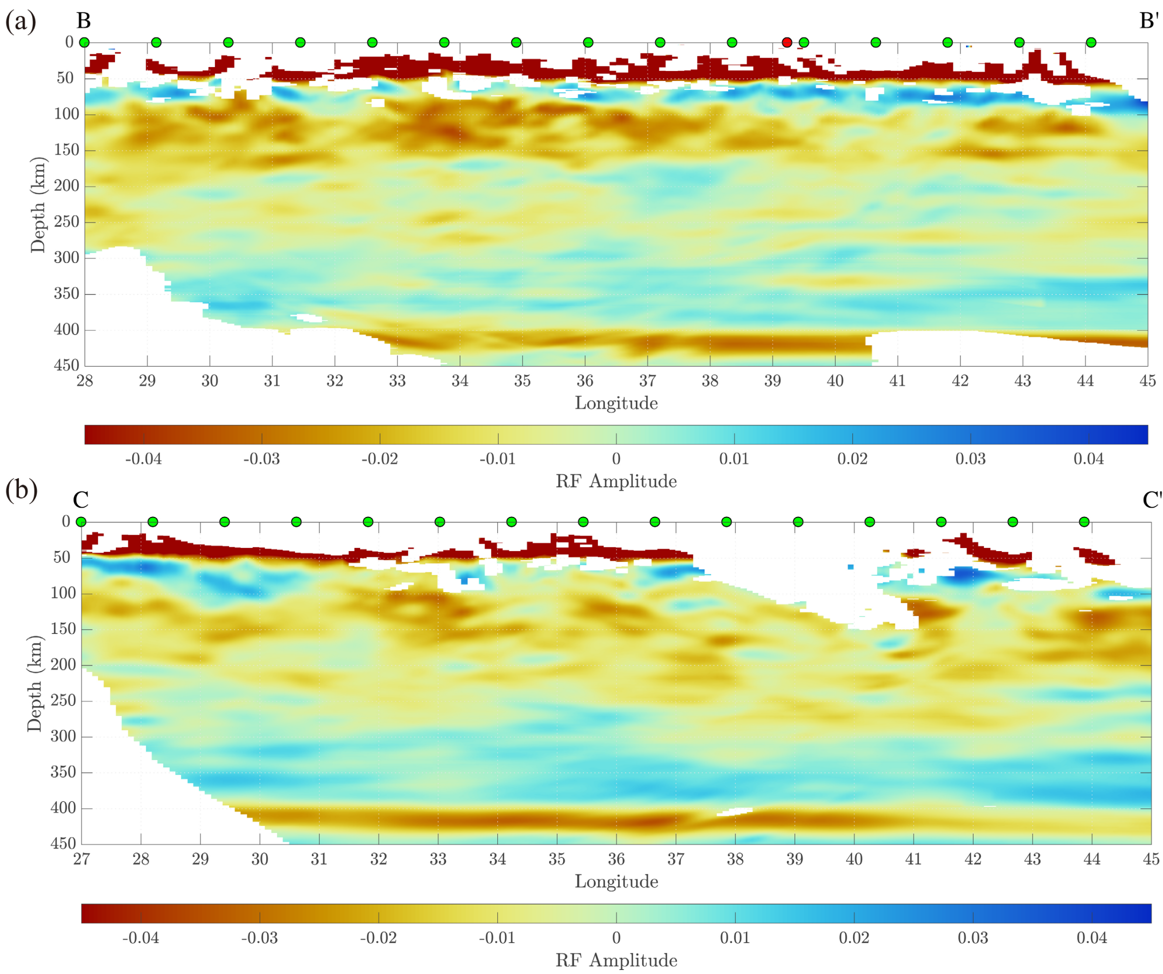

Figure 14. Sp CCP stack amplitudes on east-west profiles B-B’ and C-C’. Symbols and notations identical to Figure 11a. (a) Profile B-B’ is located at 38.4°N, and the length of the profile is 1,479 km. (b) Profile C-C’ is located at 41.6°N, and the length of the profile is 1,494 km. Profile locations shown in Figure 1.

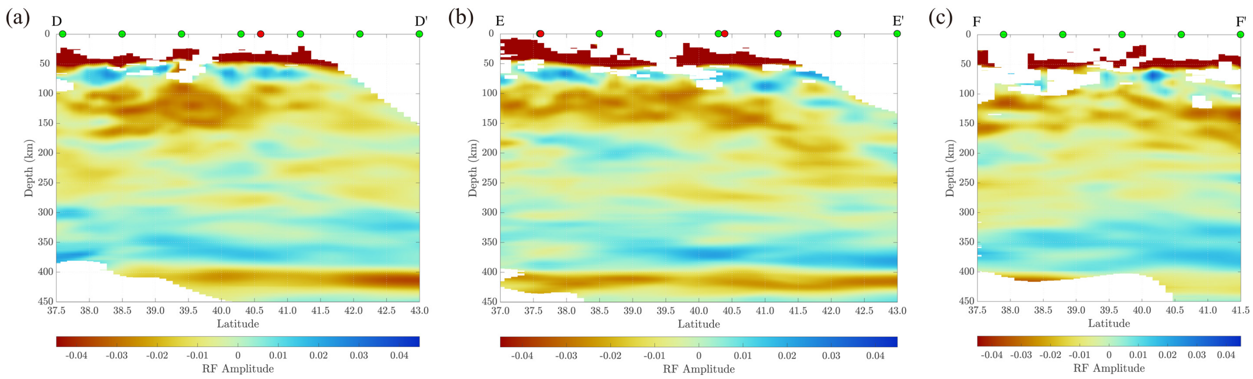

Figure 15. Sp CCP stack amplitudes on north-south oriented profiles D-D', E-E' and F-F'. Symbols and notations identical to Figure 11a, but horizontal axes are labeled with latitude. (a) Profile D-D' is located at 31.18°E, and the length of the profile is 612 km. (b) Profile E-E' is located at 37.35°E, and the length of the profile is 667 km. (c) Profile F-F' is located at 44°E, and the length of the profile is 445 km. Profile locations shown in Figure 1.

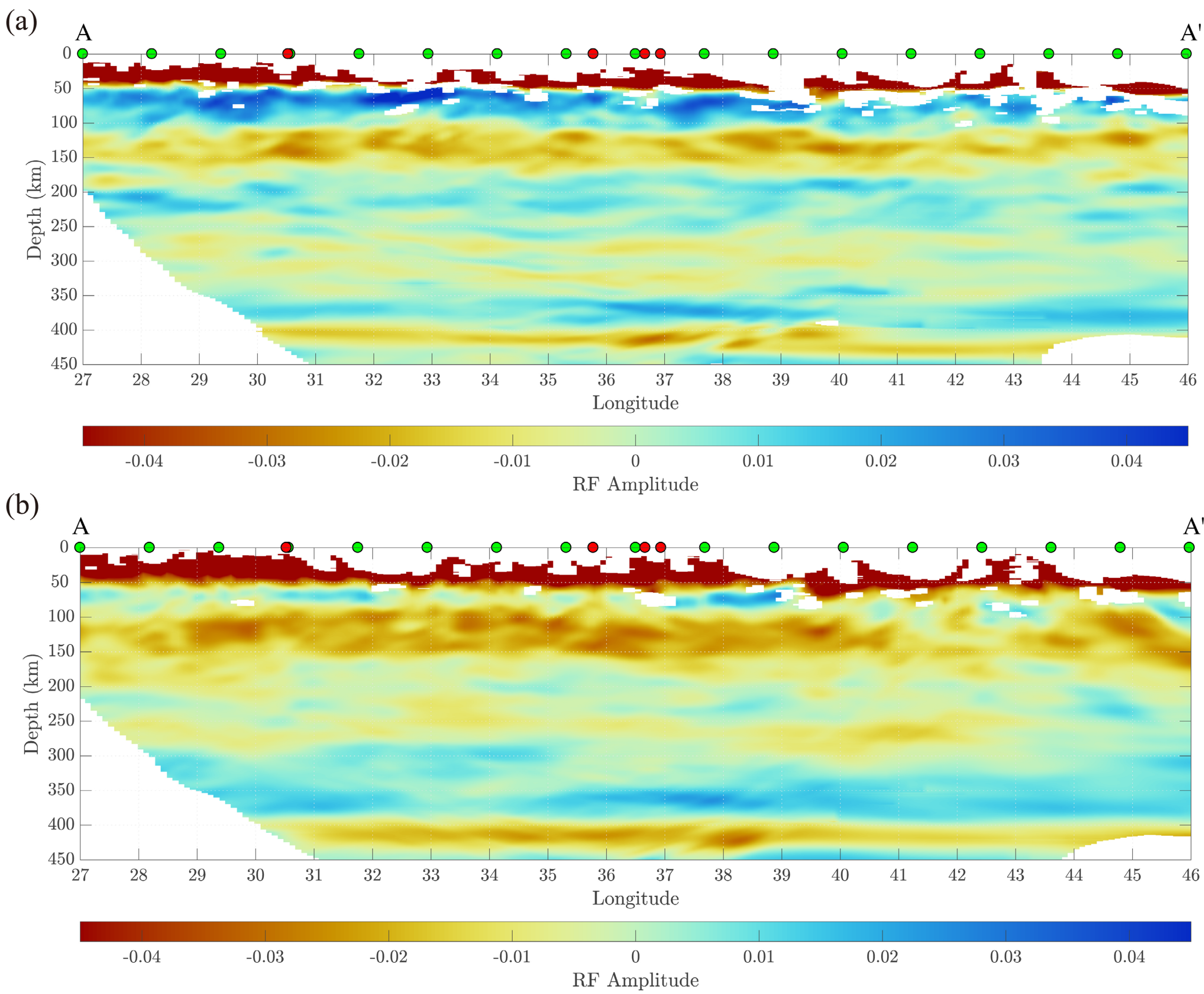

Figure 16. (a) Similar to Figure 11a but using a 2 to 20 s bandpass filter before deconvolution. Clear LAB phases are observed around ~70 km depth. (b) Similar to Figure 11a but using a 10 to 100 s bandpass filter.

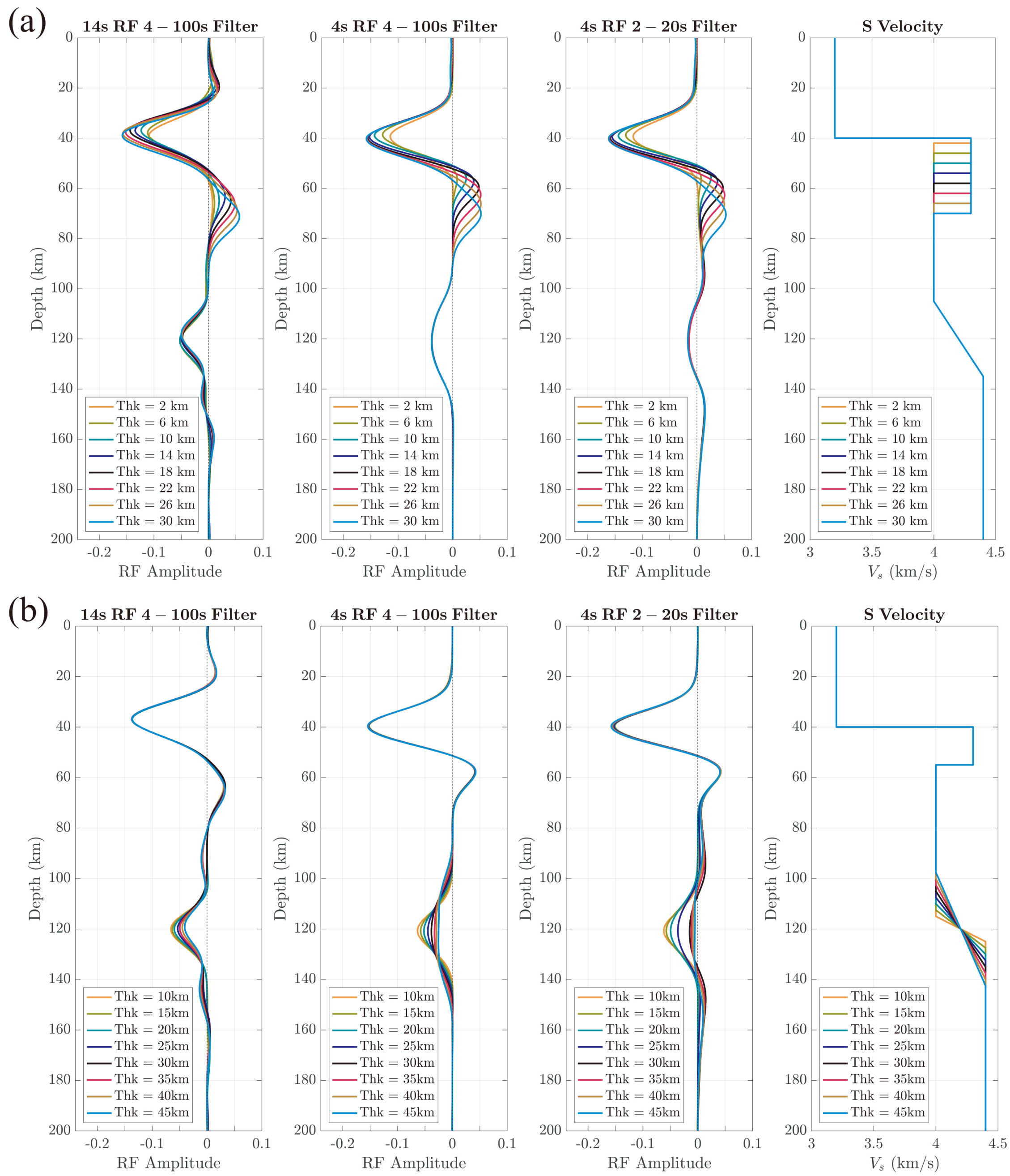

Figure 17. The frequency dependence of Sp receiver functions. (a) Synthetic Sp receiver functions for velocity models with varying mantle lithosphere thickness from 2 km to 30 km as indicated by the legend. The S waves have a ray parameter of 0.1098 s/km. Shear velocity structures are shown in the right-most panel and the mantle lithosphere is characterized by a high velocity layer starting from 40 km depth. The left-most panel shows receiver functions calculated from synthetic seismograms whose source-time functions are characterized by Gaussian first derivatives peaked at 14 s (~0.07 Hz). These waveforms were filtered with a 4 to 100 s bandpass filter before deconvolution. The middle-left panel is similar to the left-most one, but with source-time functions whose Gaussian first derivatives are peaked at 4 s (0.25 Hz). The middle-right

panel is similar to the middle-left one, but with a 2 to 20 s bandpass filter. The LAB phase is larger amplitude for the cases where the source-time function has a 4 s period. (b) Sp receiver functions for structures where the positive velocity gradient at the base of the low velocity asthenosphere at 120 km has a varying depth extent. Velocity increases from 4.0 km/s to 4.4 km/s within a layer as thin as 5 km to as broad as 45 km and, as indicated by the legend. The panels are arranged in the same way as in (a). Gradual positive velocity gradients (30-45 km depth extents) produce significant phases in seismograms with short-period (4 s) source-time function seismograms and the 4-100 s filter, but the amplitudes of these phases are reduced with the 2-20 s filter.

AGU PUBLICATIONS

Journal of Geophysical Research: Solid Earth

Supporting Information for

New Approaches to Multifrequency Sp Stacking Tested in the Anatolian Region

J. Hua[1] (junlin_hua@brown.edu), K. M. Fischer[1], M. Wu[1] and N. Blom[2]

[1] Department of Earth, Environmental and Planetary Sciences, Brown University, Providence, RI 02906, USA.

[2] Bullard Laboratories, Department of Earth Sciences, University of Cambridge, Madingley Rise, Cambridge CB3 0EZ, UK.

Contents of this file

Figures S1 to S9

Introduction

This file contains the supplementary figures for the article. Methods used to generate these figures and their interpretation are discussed in the main text.

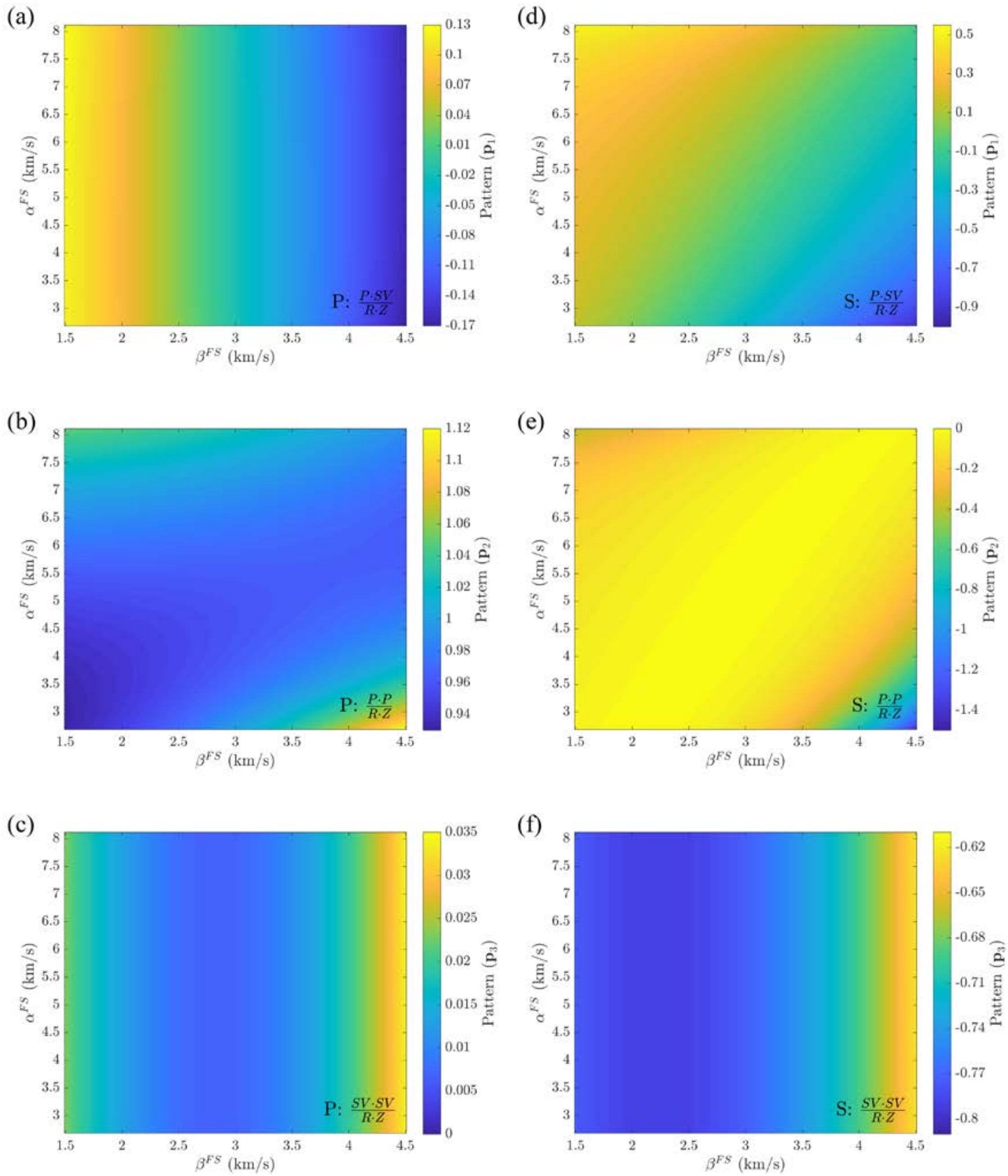

Figure S1. (a)-(c) Particle motion patterns similar to Figures 3a to 3c, but for the real P arrival used in Figure 4. (d)-(f) Particle motion patterns similar to Figures 3e to 3g, but for the real S arrival used in Figure 3. Colors show the value of the pattern for varying α^{FS} and β^{FS}; (a) $\mathbf{C}_1$ pattern; (b) $\mathbf{C}_2$ pattern, (c) $\mathbf{C}_3$ pattern for P arrivals; (d) $\mathbf{C}_1$ pattern; (e) $\mathbf{C}_2$ pattern, (f) $\mathbf{C}_3$ pattern for S arrivals. The label in the bottom right corner indicates the arrival phase and the equation for the pattern.

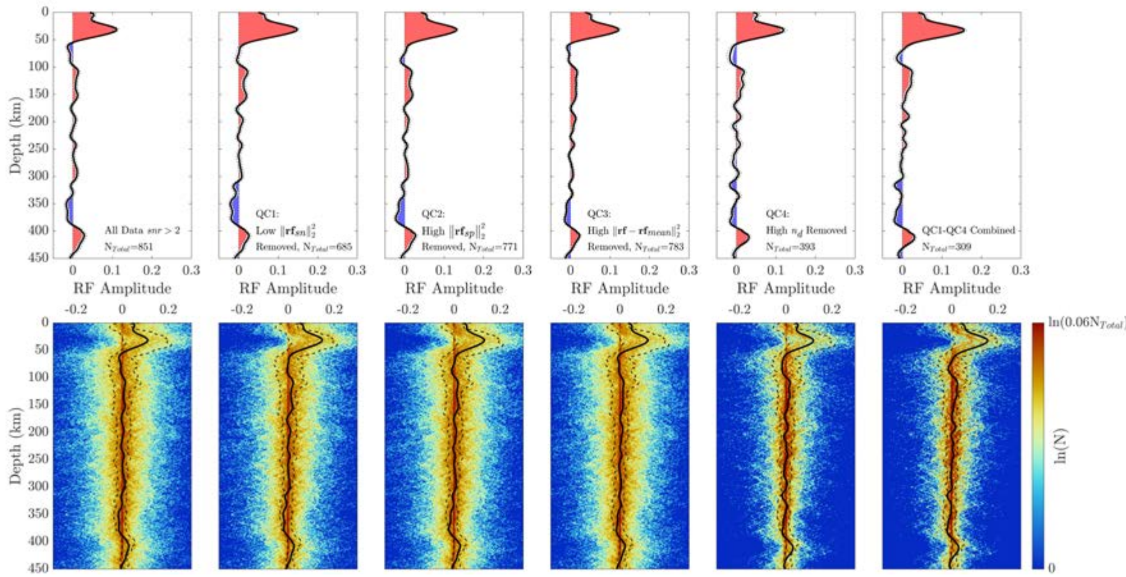

Figure S2. Effects of data quality criteria (QC) on receiver functions from the station ANTO (IU network) located at 39.87°N, 32.79°E. Sp receiver function amplitudes have their signs flipped in this figure to match the Ps convention. The first row shows stacked receiver function amplitudes migrated with the 1D velocity model at the station from Blom et al. (2020). The black solid line shows the stacked receiver function amplitude, while the dashed lines indicate one standard deviation uncertainties. Standard deviations are calculated based on eq. (26) while weighting all receiver functions equally. Red phases represent positive velocity gradients and blue phases represent negative velocity gradients. The second row shows the natural logarithm of the number of receiver functions that lie within a given depth-amplitude pixel, so these plots illustrate the distribution of individual receiver functions. Black solid lines show the stacked receiver function amplitude as in the first row, and black dashed lines show $\mathbf{rf}_{\min}$ and $\mathbf{rf}_{\max}$ obtained from the synthetic seismograms with the Blom et al. (2020) model. Panels in this row have a different amplitude scale on their horizontal axes than those in the first row, and the color bar is from 0 (one or no waveform) to $\ln(0.06N_{Total})$. N_{Total} is the number of receiver functions that pass the quality control and are used for the stack, and its value is labelled in the first row. The six columns illustrate the effects of different data quality criteria. The first column is based on all data that satisfy the signal-to-noise ratio higher than 2 requirement, while other columns also satisfy this requirement in addition to the labelled criteria. The second column has receiver functions with small $\|\mathbf{rf}_{sn}\|_2^2$ removed; the third column has ones with large $\|\mathbf{rf}_{sp}\|_2^2$ removed; the fourth column has ones with large $\|\mathbf{rf} - \mathbf{rf}_{mean}\|_2^2$ removed; the fifth column has ones with large n_d removed; and the sixth column shows the combined effect of all quality controls from column 2 to 5. Panels in the first row are labelled by the quality criterion and the number of receiver functions that pass (bottom right corner). The quality criteria are described in Section 3.

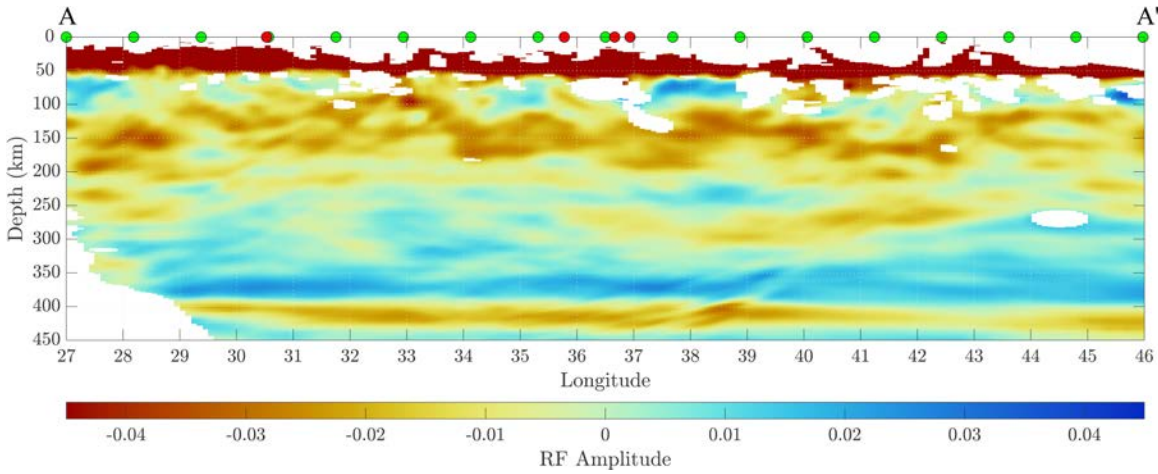

Figure S3. Sp CCP stack amplitudes on profile A-A', with symbols and notations the same as in Figure 11a. The stack is obtained with all receiver functions that pass the two Moho related quality controls which remove data with small $\|\mathbf{rf}_{sn}\|_2^2$ or large $\|\mathbf{rf}_{sp}\|_2^2$, as described in Section 3. With only the Moho criteria, we retain 45,872 receiver functions, approximately twice the number as in the final version of the stack which is shown in Figure 11a. Both versions of the stack (Figure 11a versus this figure) contain the same overall features. However, the negative phase at 80-150 km is less coherent here, illustrating the usefulness of the additional quality criteria employed in Figure 11a.

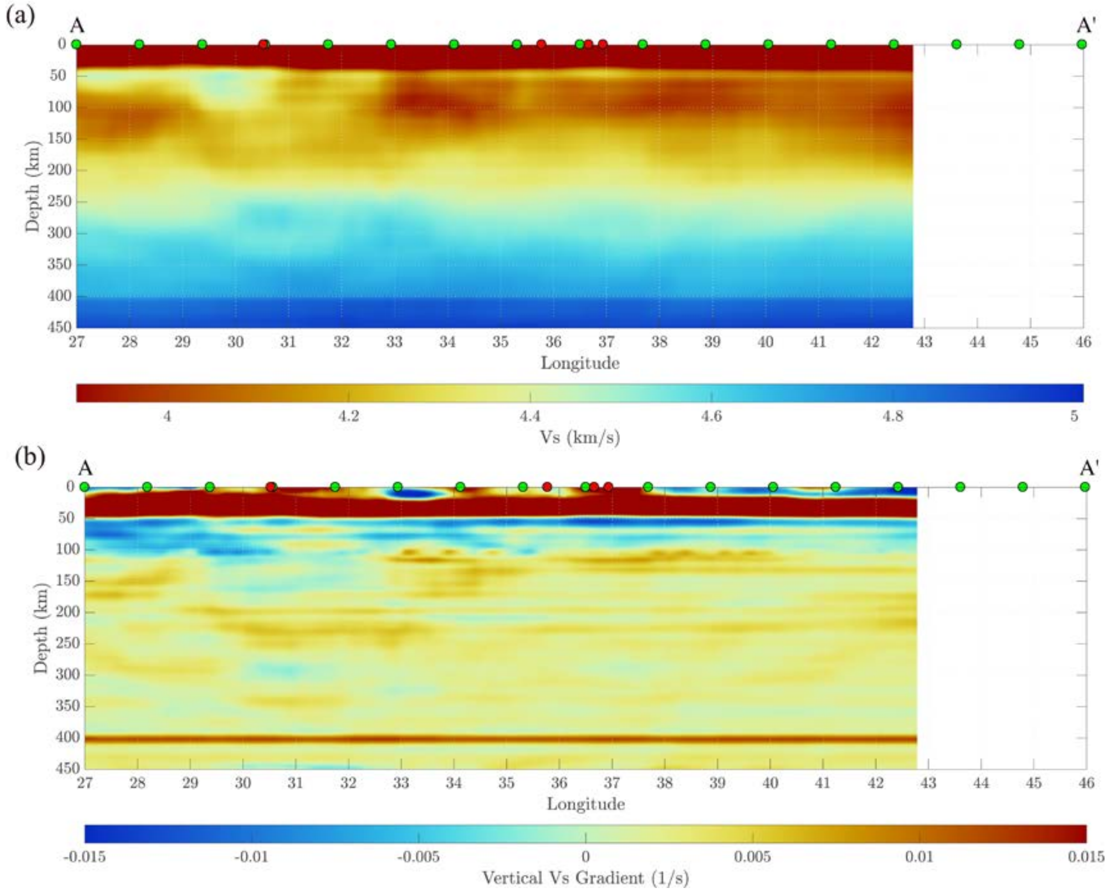

Figure S4. Shear velocity model on profile A-A'. (a) Shear wave velocity from Fichtner et al. (2013). Velocities exceeding the limit of the color bar are shown by the color at the limit (e.g. crustal velocity). (b) Vertical shear wave velocity gradient from Fichtner et al. (2013) smoothed over a 5 km depth window. The velocity model is consistent with the negative Sp phase at depths of 80 – 150 km, in the sense that the velocity model contains a low velocity layer above 150 km depth and positive velocity gradients from 33°E to 40°E at 100 – 130 km depths, but no clear gradients east of 40°E. However, the strong positive velocity gradient at 230 km depth from 29°E to 33°E in the velocity model does not correspond to a feature in the Sp CCP stack.

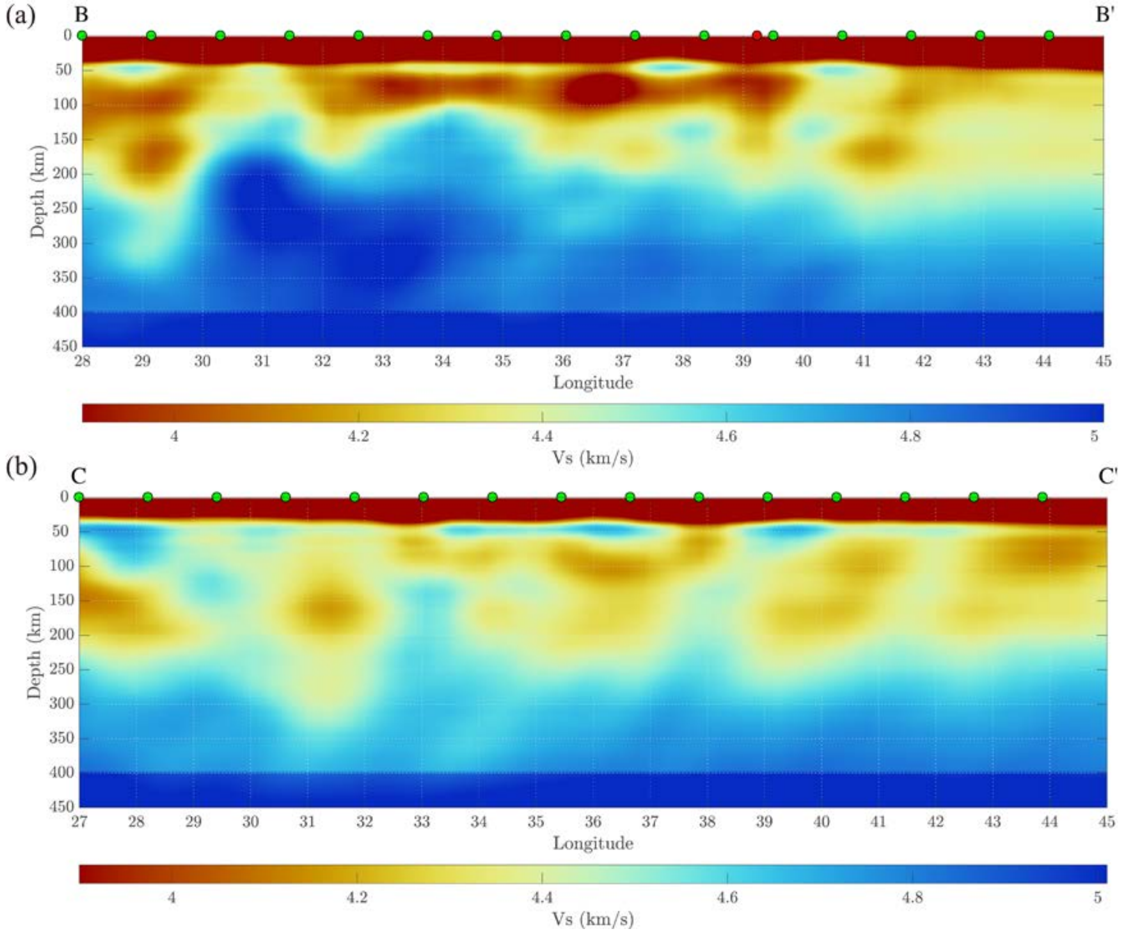

Figure S5. Shear velocity model on east-west profiles B-B' and C-C' from Blom et al. (2020). Similar to Figure 13a. Velocities exceeding the limit of the color bar are shown by the color at the limit (e.g. crustal velocities). The low velocity layer at 50-110 km depth in (a) broadly agrees with the observed positive velocity gradient in Figure 14a. The absence of a strong low velocity anomaly in (b) agrees with the lack of negative Sp phases in Figure 14b.

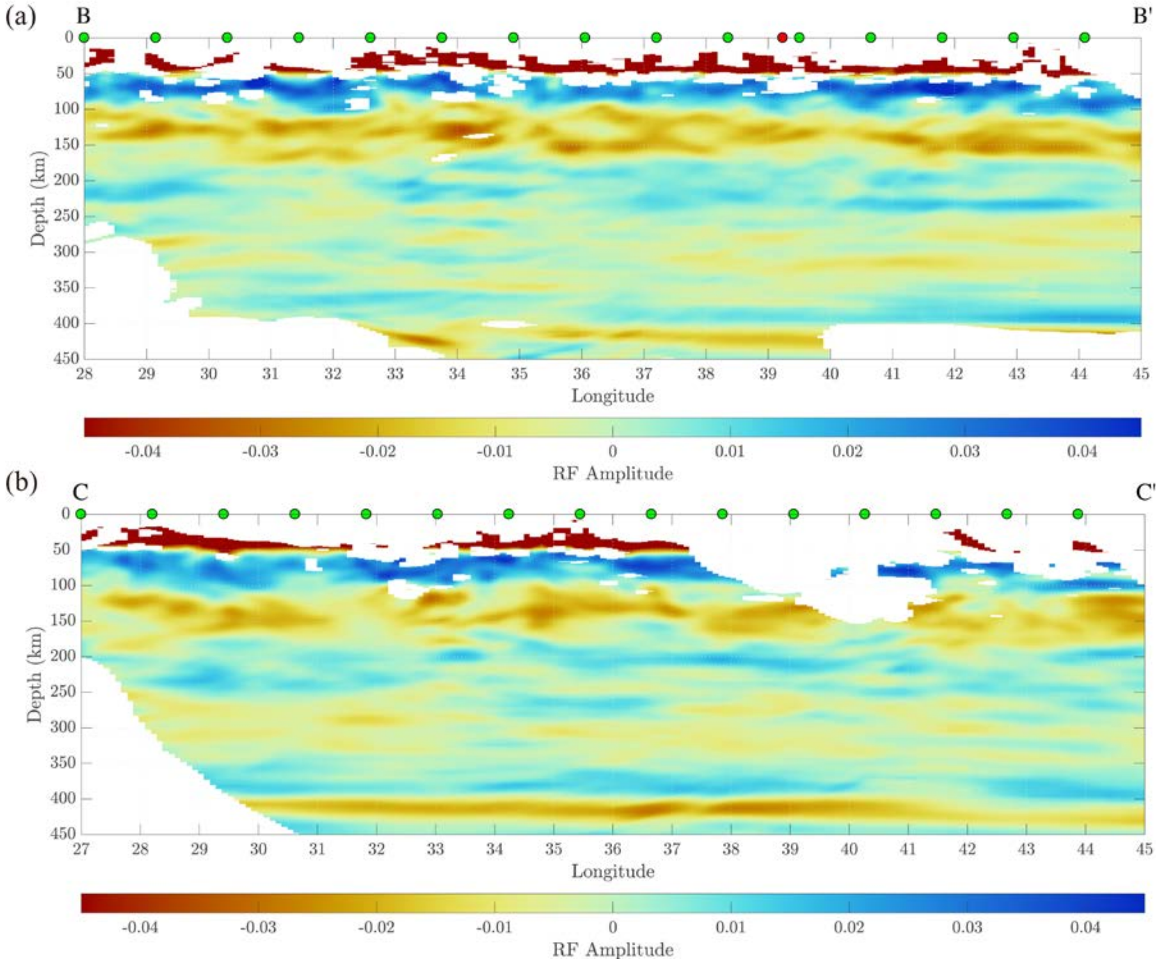

Figure S6. Sp CCP stack amplitudes on east-west profiles B-B' and C-C'. Similar to Figure 14, but using the 2-20 s bandpass filter before deconvolution which is also used in Figure 16a. Symbols and notations identical to Figure 11a. Profile locations shown in Figure 1.

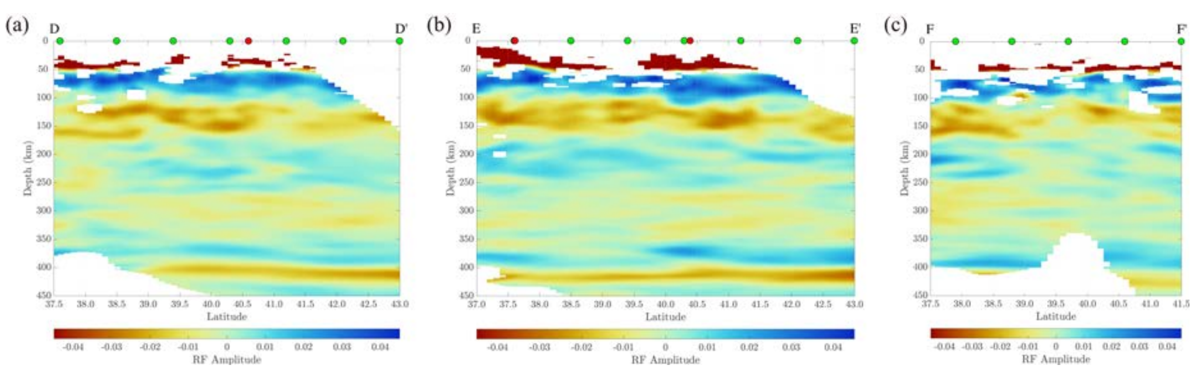

Figure S7. Sp CCP stack amplitudes on north-south oriented profiles D-D', E-E' and F-F'. Similar to Figure 15, but using a 2-20 s bandpass filter before deconvolution. Symbols and notations identical to Figure 11a, but horizontal axes are labeled with latitude. Profile locations shown in Figure 1.

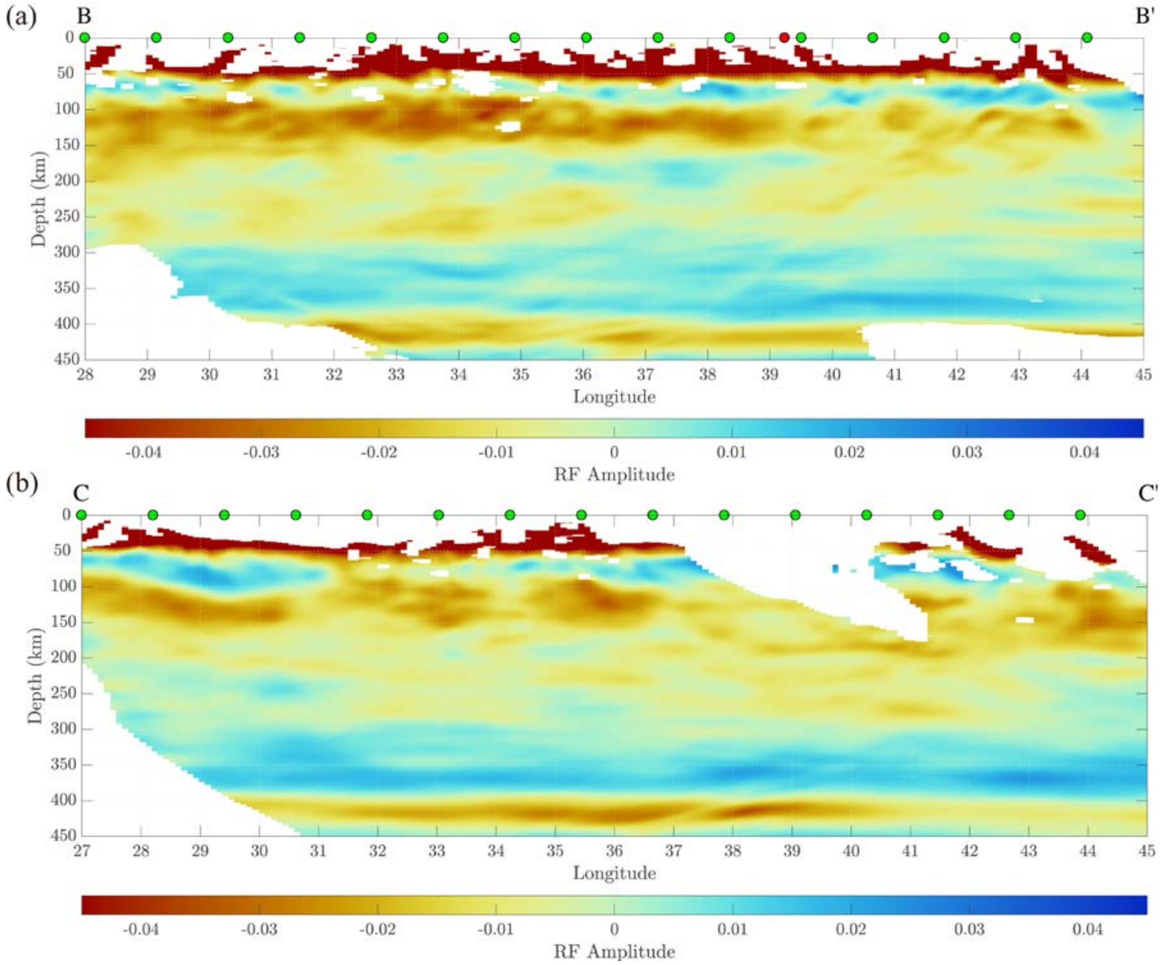

Figure S8. Sp CCP stack amplitudes on east-west profiles B-B' and C-C'. Similar to Figure 14, but using the 10-100 s bandpass filter before deconvolution which is also used in Figure 16b. Symbols and notations identical to Figure 11a. Profile locations shown in Figure 1.

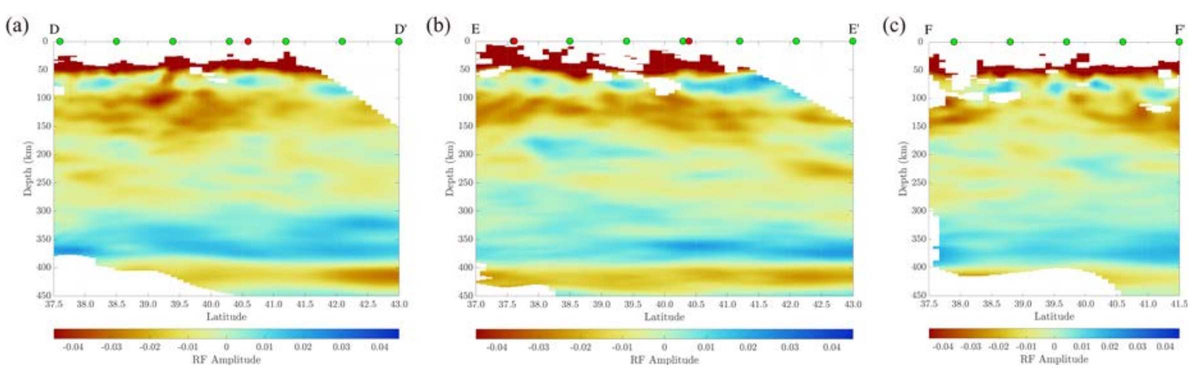

Figure S9. Sp CCP stack amplitudes on north-south oriented profiles D-D', E-E' and F-F'. Similar to Figure 15, but using a 10-100 s bandpass filter before deconvolution. Symbols and notations identical to Figure 11a, but horizontal axes are labeled with latitude. Profile locations shown in Figure 1.